Search for a scalar dimuon resonance with LHC Run2 data from the ATLAS detector

Georg Friedrich Hönig

SIGILL·UNIVERSITAT·LUDOVIC·MAXIM

München 2017

Search for a scalar dimuon resonance with LHC Run2 data from the ATLAS detector

Georg Friedrich Hönig

Dissertation
an der Fakultät für Physik
der Ludwig–Maximilians–Universität
München

vorgelegt von
Georg Friedrich Hönig
aus Weißenburg in Bayern

München 2017

Erstgutachter: Prof. Dr. Dorothee Schaile

Zweitgutachter: Prof. Dr. Thomas Kuhr

Tag der Abgabe: 10. März 2017
Tag der mündlichen Prüfung: 21. April 2017

Zusammenfassung

Diese Analyse stellt die Suche nach einem Higgs-artigen Boson vor, das in entgegengesetzt geladene Myonen zerfällt. Das invariante Massenspektrum des Dimyonsystems wird nach einem Peak oberhalb der Z-Resonanz hin untersucht, der von $\mathrm{H} \rightarrow \mu\mu$ stammt. Die zwei berücksichtigten Produktionsmechanismen des Higgs-Bosons sind Gluon-Gluon-Fusion (ggF) und Vektorboson-Fusion (VBF). Letztere weist in ihrem Endzustand zwei zusätzliche Jets auf. Der dominante Hintergrund stammt vom Z/Drell-Yan Prozess.

Diese Arbeit benutzt Daten, die im Jahr 2015 vom ATLAS Detektor am LHC während Proton-Proton-Kollisionen bei einer Schwerpunktsenergie von 13 TeV aufgezeichnet wurden. Die analysierte Datenmenge enspricht einer integrierten Luminosität von $3.2\,\mathrm{fb}^{-1}$.

Ereignisse werden anhand ihrer kinematischen Merkmale in sieben Regionen mit erhöhtem Signalanteil eingeteilt. Eine der Regionen zielt hauptsächlich auf VBF-Produktion ab, während die anderen darauf optimiert sind, die uneinheitliche Massenauflösung des Detektors auszunutzen.

Die Form des Hintergrundspektrums wird auf der Basis von Monte-Carlo-Simulationen untersucht und eine parametrisierte Funktion entwickelt, um sie zu beschreiben. Zusätzlich wird die Form und Normierung des Signalpeaks in den verfügbaren simulierten Datensätzen für gegebene Higgs-Massen mittels einer parametrisierten Funktion modelliert. Aus der Interpolation der zugehörigen Parameter ergeben sich Signaltemplates für Hypothesen beliebiger Higgs-Massen.

Ein kombinierter Fit des Signal- und Hintergrund-Modells wird in den sieben Signalregionen durchgeführt, um sowohl die Hintergrundabschätzung als auch das gemessene Signal zu extrahieren.

Kein signifikanter Überschuss über der Erwartung dessen, was das Standard Modell ohne den $\mathrm{H} \rightarrow \mu\mu$ Zerfall vorhersagt, wurde in den analysierten Daten beobachtet. Ausschlussgrenzen an die Signalstärke auf dem 95% Konfidenzniveau werden als Funktion der Higgsmasse im Bereich von 115 GeV bis 145 GeV gelegt. Dieses Ergebnis wird zusätzlich als Ausschlussgrenze an das Produkt von Wirkungsquerschnitt und Verzweigungsverhältnis des Zerfalls eines allgemeineren skalaren Bosons interpretiert, das in Myonpaare zerfällt.

Abstract

This analysis presents the search for a Higgs-like Boson decaying into a pair of oppositely charged muons. The invariant mass spectrum of the dimuon system is investigated for a peak above the Z-resonance arising from $\mathrm{H} \rightarrow \mu\mu$ decays. The two considered production mechanisms for the Higgs boson are gluon-gluon fusion (ggF) and vector boson fusion (VBF), the latter featuring two additional jets in its final state. The dominant background arises from the Z/Drell-Yan process.

This thesis uses data taken by the ATLAS detector at the LHC during proton-proton collisions at a center of mass energy of $13\,\mathrm{TeV}$ in 2015. The amount of data analyzed corresponds to an integrated luminosity of $3.2\,\mathrm{fb}^{-1}$.

Events are selected on the basis of their kinematic features into a total of seven regions with enhanced signal contribution. One of the region targets primarily VBF production, while the others are optimized to take advantage of varying mass resolution of the detector.

The shape of the background spectrum is studied based on Monte Carlo simulations and a parametrized fit function is developed to describe it. In addition, the shape and normalization of the signal peak for the set of available simulated Higgs mass points is modeled by another parametrized fit function. Interpolating the associated parameters yields signal templates for arbitrary Higgs mass hypotheses.

A combined fit of the signal and background model to data is performed in the seven signal regions to extract both the background estimation and the measured signal.

No significant excess above the expectation from the Standard Model without the $\mathrm{H} \rightarrow \mu\mu$ decay has been observed in the analyzed data. A 95% confidence exclusion limit is set on the signal strength as a function of Higgs mass in the range between $115\,\mathrm{GeV}$ and $145\,\mathrm{GeV}$. This result is re-interpreted as a limit on cross section times branching ratio for the decay of a more general scalar boson decaying into muon pairs.

Contents

Chapter 1

Introduction

The Standard Model (SM) of particle physics represents the currently best understanding of almost all known phenomena in particle physics. It offers an exceptionally good description of all known particles of matter and their interactions via the electromagnetic, weak and strong forces. The SM does not incorporate the fourth fundamental force of nature, gravity, as described by general relativity.

A key component in the SM is the Engler-Brout-Higgs mechanism, which spontaneously breaks the electroweak gauge symmetry of the theory. Without it the theory would predict massless W and Z bosons in direct contradiction to experimental observations. This mechanism also leads to the prediction of a new heavy scalar particle called the Higgs boson H.

A decades long search for the Higgs boson as the final piece of the SM followed. Searches [1] at the Large Electron Positron Collider (LEP) combining measurements from the ALEPH, DELPHI, L3 and OPAL experiments showed the Higgs boson mass had to be greater than 114.4 GeV, but could not discover the boson itself.

The Large Hadron Collider at CERN, the successor of LEP, and its associated experiments were then designed with finding the Higgs boson as one of the main goals in mind. In July 2012 both the ATLAS [2] and CMS [3] collaborations at the LHC announced the discovery of a new particle with a mass of approximately 125 GeV. So far all the properties of this particle that have been studied are consistent with the SM Higgs boson. The precise value of the Higgs boson mass is measured to be $m_{\mathrm{H}} = 125.09 \pm 0.21(stat.) \pm 0.11(syst.)$ GeV [4].

Since deviations could hint at new physics beyond the SM, the next important goal for the LHC is the determination of all the couplings between the Higgs boson and the other SM particles. The efforts in this direction so far [5] show no significant deviations so far. A particular challenge is the measurement of the couplings fermions, especially of the first and second generations. Apart from $H \to b\bar{b}$ and $H \to \tau^+\tau^-$, which involves third generation fermions, $H \to \mu^+\mu^-$ is a fermionic Higgs decay accessible at the LHC and is the topic of this analysis. It offers a clean final state where Higgs couplings to second generation fermions can be measured. A previous search at ATLAS [6] yielded a 95% confidence observed upper limit of the $\mathrm{H} \to \mu\mu$ decay of 7.0 times the SM prediction, and at CMS [7] of 7.4, both for an assumed Higgs mass of $m_{\mathrm{H}} = 125$ GeV.

In this thesis, a search for Higgs boson decays into muon-antimuon pairs is presented. The data used has been collected by the ATLAS detector in 2015 from proton-proton collisions at the LHC with a center of mass energy of 13 TeV. A fit-based method is described to derive an upper limit on the signal strength of the $\mathrm{H} \rightarrow \mu\mu$ process for assumed Higgs masses between 110 GeV and 150 GeV.

Chapter 2

Theoretical Background

The Standard Model of Particle Physics (SM) is the theory that describes our current understanding of particle physics [8]. It was largely formulated in the 1960s and 1970s in a number of seminal papers [9][10][11][12][13]. It encompasses all particles of matter in the form of fermions, and the interactions between them, mediated by bosonic force carriers.

The SM electroweak theory consists of two gauge theories: Electroweak (EW) theory unifying electromagnetic and weak theories, and quantum chromodynamics (QCD). EW symmetry is broken in the SM by the Brout-Englert-Higgs (BEH) mechanism [14][15][16], which gives rise to the Higgs boson. This chapter gives a short overview over the SM and the BEH mechanism in particular.

2.1 The Standard Model

According to the SM, matter is composed of fermions, i.e. particles with half-integer spin. They are excitations of three generations of fermionic fields. Each generation has one charged lepton, a corresponding neutrino and two quarks, one up-type and one down-type, with three possible colors for each quark. An anti-partner of the same mass also exists for each of those particles. Table 2.1 gives an overview of all SM matter particles.

The interactions between the matter particles are mediated by bosons, which are particles with integer spin. Electroweak interactions are mediated by the massless photon and the massive $W^{\pm}$ and Z bosons, while massless gluons are responsible for strong interactions. Lastly the BEH mechanism, which generates the masses of vector bosons and fermions, leads to another particle called the Higgs boson as an excitation of the Higgs field. Table 2.2 lists these bosons and their basic properties. However gravity as a fundamental force of nature is not incorporated in the SM.

The Standard Model is formulated in terms of quantum field theories [18], specifically quantum chromodynamics (QCD) describing strong interactions, and electroweak (EW) theory unifying the description of both electromagnetic and weak interactions.

Analogous to classical Lagrangian mechanics, the dynamics of a system in quantum field theory is described by a Lagrangian density function $\mathcal{L}$. It is a function of the fields

First generation	Fermion	Symbol	Charge
Quarks	Up quark	u	$+2/3$
	Down quark	d	$-1/3$
Leptons	Electron	e	-1
	Electron neutrino	ν_e	0
Second generation	Fermion	Symbol	Charge
Quarks	Charm quark	c	$+2/3$
	Strange quark	s	$-1/3$
Leptons	Muon	μ	-1
	Muon neutrino	ν_μ	0
Third generation	Fermion	Symbol	Charge
Quarks	Top quark	t	$+2/3$
	Bottom quark	b	$-1/3$
Leptons	Tau	τ	-1
	Tau neutrino	ν_τ	0

Table 2.1: The fundamental fermions of the SM and their basic properties [17]

Boson	Symbol	Force	Charge
Photon	γ	electromagnetic	0
Gluon	g	strong	0
W boson	$W^{\pm}$	weak	± 1
Z boson	Z	electroweak	0
Higgs boson	H	Higgs field	0

Table 2.2: The fundamental bosons of the SM and their basic properties [17]

ϕ, the four space time coordinates x_μ, $\mu \in \{0, 1, 2, 3\}$, and the derivatives of the fields $\frac{\partial \phi}{\partial x_\mu}$. From the principle of least action, i.e. the minimum of the integral over $\mathcal{L}$, follows the Euler-Lagrange equation, which determines the dynamics of the system.

$$\frac{\partial}{\partial x^\mu}\left(\frac{\partial \mathcal{L}}{\partial(\partial\phi/\partial x^\mu)}\right) - \frac{\partial \mathcal{L}}{\partial \phi} = 0 \tag{2.1}$$

A simple example is the Lagrangian for a field with spin 0:

$$\mathcal{L} = \frac{1}{2}(\partial_\mu \phi)(\partial^\mu \phi) - \frac{1}{2}m^2\phi^2 \tag{2.2}$$

Applying the Euler-Lagrange equation above leads to the Klein-Gordon equation for a free scalar particle

$$(\partial_\mu \partial^\mu + m^2)\phi = 0. \tag{2.3}$$

The full SM Lagrangian consists of the free particle Lagrangians of the SM particles, and terms describing their interactions. To describe the interactions, local gauge invariance is imposed. This is the requirement that the Lagrangian has to be invariant under the transformation

$$\phi \to e^{-i\alpha^i(x)\cdot f^i}\phi, \tag{2.4}$$

where $\alpha^i(x)$ are arbitrary functions of space time, hence local gauge transformation, and f^i are the generators of the gauge symmetry group of the fields ϕ. The underlying symmetry group of the SM is $U(1)_Y \otimes SU(2)_L \otimes SU(3)_C$.

2.1.1 Quantum Chromodynamics

Quantum Chromodynamics is the theory of the strong force. It describes the interactions of particles carrying color charge, which are quarks and gluons. Its symmetry is $SU(3)_C$ with the index C representing color, the charge of the strong interaction. Each quark carries one of the three colors “red”, “blue” or “green”. The interactions between quarks are mediated by the massless spin-1 gluons, which carry a combination of one color and one anti-color as their charge. Never have any free colored particles been found in nature. This means quarks must always form colorless bound states in a phenomenon called confinement. These hadrons come in form of mesons, a bound state of two quarks which have between them one color and the associated anti-color, and baryons which consist of three quarks with one of the three different colors each. Single partons (quarks or gluons) produced in particle interactions never emerge from the interaction point as such, but form a shower of uncolored hadrons traveling in the same direction, collectively called a jet. The probability density function of finding a parton with forward momentum fraction x at a certain energy scale in a hadron is called its parton distribution function (PDF).

The QCD Lagrangian for the fermionic fields Ψ and gauge fields $\mathbf{G}_\mu$ can be written as

$$\mathcal{L}_{QCD} = \bar{\Psi}(i\gamma_\mu \mathcal{D}^\mu - m)\Psi - \frac{1}{4}\mathbf{G}_{\mu\nu}\mathbf{G}^{\mu\nu}, \tag{2.5}$$

where γ_μ are the Dirac matrices and $\mathbf{G}_{\mu\nu}$ is the field strength tensor of the gauge fields.

The covariant derivative $\mathcal{D}_\mu$ encapsulates the dynamics of the fermionic fields and their interaction with the gluons, and is defined as

$$\mathcal{D}_\mu = \partial_\mu + \frac{1}{2} i g_s \lambda \cdot \mathbf{G}_\mu \tag{2.6}$$

where g_s is the strong coupling constant and λ the eight Gell-Mann matrices, the generators of $SU(3)$.

2.1.2 Electroweak Theory

Electroweak theory is a joint description of both electromagnetic and weak interactions based on the $SU(2)_L \otimes U(1)$ symmetry group [19]. It has four initially massless gauge fields. The first one, called B_μ, corresponds to the $U(1)$ group and couples to weak hypercharge, defined as

$$Y = 2(Q - I_3) \tag{2.7}$$

where Q is the electric charge and I_3 the third component of the weak isospin.

The other three are W_μ^1, W_μ^2, and W_μ^3 from $SU(2)_L$, coupling to weak isospin. The index L indicates, that the weak interaction only acts on left-handed fermions and right-handed anti-fermions.

The Lagrangian of the electroweak theory reads as

$$\mathcal{L}_{EW} = \sum_k i\bar{\psi}\gamma^\mu \mathcal{D}_\mu \psi_k - \frac{1}{4}\mathbf{W}_{\mu\nu}\mathbf{W}^{\mu\nu} - \frac{1}{4}B_{\mu\nu}B^{\mu\nu}, \tag{2.8}$$

where the ψ_k denote the different quark and lepton flavors. The covariant derivative for left-handed particles is

$$\mathcal{D}_\mu = \partial_\mu + i\frac{g}{2}\tau \cdot \mathbf{W}_\mu + i\frac{g'}{2}B_\mu Y. \tag{2.9}$$

Here τ is a three-vector of Pauli-matrices, and $\mathbf{W}_\mu$ a three-vector made up of the three W_μ^i fields. $B_{\mu\nu}$ and $\mathbf{W}_{\mu\nu}$ are the associated field tensors.

The electroweak theory shown so far does not include masses for the gauge bosons, and adding simple mass terms to the Lagrangian would break local gauge invariance. But measurements have shown that the W and Z bosons are massive, so the electroweak symmetry has to be broken.

2.2 The BEH-Mechanism

The BEH-mechanism, or simply Higgs mechanism, offers a way to dynamically generate mass for the $W^\pm$ and Z bosons without breaking local gauge invariance. It is an example of spontaneous symmetry breaking, where a system loses symmetry in its ground state. The Higgs mechanism introduces a new complex scalar field with weak hypercharge $Y = 1$

$$\phi = \begin{pmatrix} \phi^+ \\ \phi^0 \end{pmatrix} \tag{2.10}$$

with an associated potential term

$$V(\phi) = \mu^2 |\phi^\dagger \phi| + \lambda |\phi^\dagger \phi|^2, \tag{2.11}$$

where λ is a positive real number, such that the Lagrangian becomes

$$\mathcal{L}_{Higgs} = |\mathcal{D}_\mu \phi|^2 - V(\phi) \tag{2.12}$$

There are two classes of solutions for the minimum of the potential. For $\mu^2 \geq 0$ there is only one minimum at $\phi = 0$. However, for $\mu^2 < 0$ the minimum no longer is at zero, and the field develops a vacuum expectation value $\langle \phi \rangle$ which minimizes the potential at

$$\langle \phi \rangle = \frac{1}{\sqrt{2}} \begin{pmatrix} 0 \\ v \end{pmatrix} \tag{2.13}$$

with $v = \sqrt{-\frac{\mu^2}{\lambda}}$.

The field ϕ is now rewritten in terms of an expansion around the vacuum expectation value as

$$\phi = \frac{1}{\sqrt{2}} \begin{pmatrix} 0 \\ v + H(x) \end{pmatrix} \tag{2.14}$$

The new form of the Lagrangian now shows terms that can be interpreted as the masses of $W^\pm$ and Z bosons, which themselves are linear combinations of the initial fields B_μ and W^i_μ as

$$\begin{aligned} W^\pm_\mu =& \frac{1}{\sqrt{2}}(W^1_\mu \mp i W^2_\mu) \\ Z^\mu =& \frac{-g' B_\mu + g W^3_\mu}{\sqrt{g^2 + g'^2}} \end{aligned} \tag{2.15}$$

just as the photon

$$A^\mu = \frac{g B_\mu + g' W^3_\mu}{\sqrt{g^2 + g'^2}} \tag{2.16}$$

which however remains massless. The masses are $m_\gamma = 0$, $m_W = \frac{gv}{2}$ and $m_Z = \frac{m_W}{\cos\theta_W}$, where the Weinberg angle θ_W is defined by $\tan\theta_W = \frac{g'}{g}$.

The Higgs mechanism has been introduced to solve the problem of massive gauge bosons, but it can also account for the masses of fermions via Yukawa coupling to the same Higgs field [19]. The resulting fermion masses m_f have the form

$$m_f = \frac{\lambda_f v}{\sqrt{2}} \tag{2.17}$$

with λ_f being a free coupling parameter for each fermion type.

2.3 Beyond the Standard Model

The Standard Model as it exists today is hugely successful in describing a wide range of phenomena. It is however incomplete [20] since is does not include gravity, which is described by the theory of general relativity. So far it has not been possible to integrate both theories with each other.

Furthermore there are a number of other phenomena which cannot be accommodated by the SM. Examples are the existence of dark matter, for which no particle in the SM is a suitable candidate, dark energy, and the strong asymmetry between the amount of matter and anti-matter in the universe. The SM also has free parameters like the masses of the fermions, which can experimentally measured, but the theory does not give any prediction of their actual values.

Because of this, new theories like Supersymmetry have been proposed as modifications, extensions, or alternatives to the SM. These theories generally predict deviations in the properties of the already known particles, and often the existence of additional so far undiscovered particles.

Studying the properties of the newly discovered Higgs boson, such as its couplings to its various decay product, offers an opportunity to find such a deviation, which might give an insight [21] as to the nature of physics beyond the Standard Model.

Chapter 3

Experimental Setup

3.1 The Large Hadron Collider

The Large Hadron Collider (LHC) is a hadron accelerator and collider at CERN, the European Organization for Nuclear Research. It is located underground in a 27 km long circular tunnel at the border of Switzerland and France. This tunnel has previously housed the Large Electron-Positron Collider (LEP). No other lepton collider has since surpassed LEP in terms of its center of mass energy $\sqrt{s} = 209\,\text{GeV}$.

LEP was replaced by a hadron collider of the same dimensions, which can reach a much higher center of mass energy. The LHC [22] is used to accelerate two counter-rotating beams of proton bunches up to a design energy of 7 TeV. These bunches are then intentionally made to collide at four interaction points. At each interaction point, one of the four major LHC experiments is installed: ALICE (A Large Ion Collider Experiment) is a detector designed to study the collisions of lead ions, which the LHC is sometimes used to accelerate instead of protons. LHCb (LHC beauty) is also a special purpose detector, focused on studying hadron decays containing *b*-quarks.

ATLAS (A Toroidal LHC ApparatuS) and CMS (Compact Muon Solenoid) are both general-purpose detectors. They are used to study a wide range of particle physics subjects, among them precision measurements of the SM, Higgs physics and searches for new supersymmetric or exotic particles.

3.1.1 The CERN Accelerator Complex

The LHC is the last step in a series of successive accelerators, collectively known as the CERN Accelerator Complex. The process starts with neutral hydrogen gas, which is ionized to obtain protons and then accelerated by a linear accelerator, Linac 2, up to 50 MeV. A series of synchrotron accelerators brings this energy up to 1.4 GeV, 25 GeV and finally 450 GeV. At this energy, they are injected into the LHC ring, which brings the protons up to a the maximum energy of currently 6.5 TeV. Figure 3.1 shows an overview of this complex, which also includes a number of other components used for experiments besides the LHC.

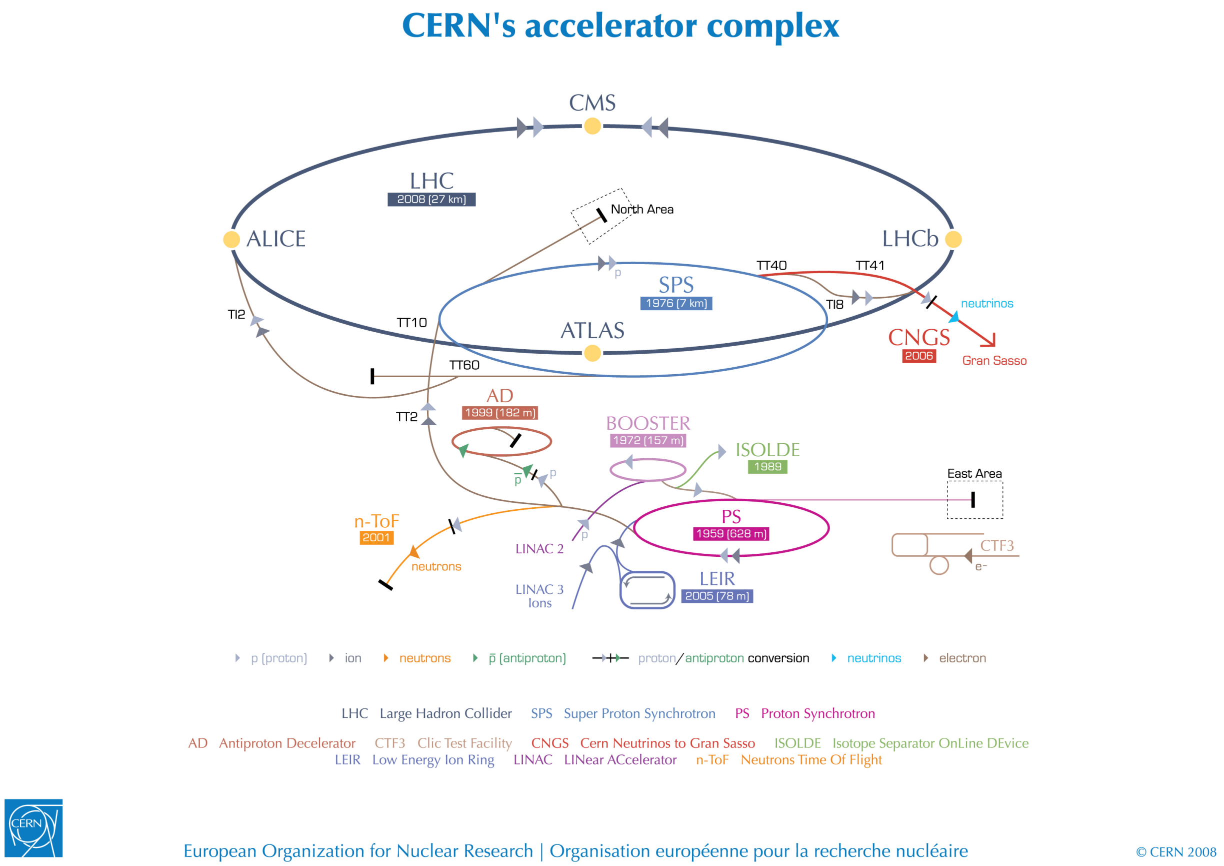

Figure 3.1: Overview of the CERN Accelerator Complex [23]

Inside the LHC, there are two separate beam pipes for the two counter-rotating beams, kept under high vacuum. Superconducting dipole and quadrupole magnets around the ring guide and focus the beams. In the beams the protons travel in bunches of about 10^{11} protons. These are traveling 25 ns apart, leading to a bunch-crossing rate of 40 MHz.

3.1.2 Luminosity and Event Rates

At the interaction points, the proton bunches are magnetically deflected in such a way that they collide almost head on, while keeping the diameter of the bunches as small as possible in order to increase the instantaneous luminosity. Such bunch crossings occur with a frequency of about 40 MHz in the center of each experiment.

The total rate of proton-proton collisions is given as $f = \sigma \cdot \mathcal{L}$, where the instantaneous luminosity $\mathcal{L}$ can be written [24] as

$$\mathcal{L} = \frac{n_b f_r n_1 n_2}{2\pi \Sigma_x \Sigma_y} \tag{3.1}$$

Here f_r is the revolution frequency of the bunches in the LHC, n_1 and n_2 are the numbers of protons in one bunch for each beam. Σ_x and Σ_y are the widths of the beams in x and y direction; they are determined in van-der-Meer scans. In the van-der-Meer method [25], the two LHC beams are moved through each other in order to determine the size of the beams in the interaction region.

The cross section σ is a measure for the probability of a collision occurring at a bunch crossing of protons with a certain energy. It gets its name from its interpretation as an effective area of a proton that can be hit by another proton. All processes which can occur at a proton-proton collision have their own corresponding cross section. Together they sum up to the total cross section σ. An overview of some proton-proton cross sections as a function of center of mass energy is given in figure 3.2.

The total number of events of a process is then $N = \sigma \cdot L$, where L is the time integrated luminosity $L = \int dt \cdot \mathcal{L}$. It can be used as a measure of the amount of data that was taken during the corresponding time. During the data taking at $\sqrt{s} = 13$ TeV in 2015, an amount of data usable for this analysis was taken corresponding to 3.2 fb^{-1} of integrated luminosity.

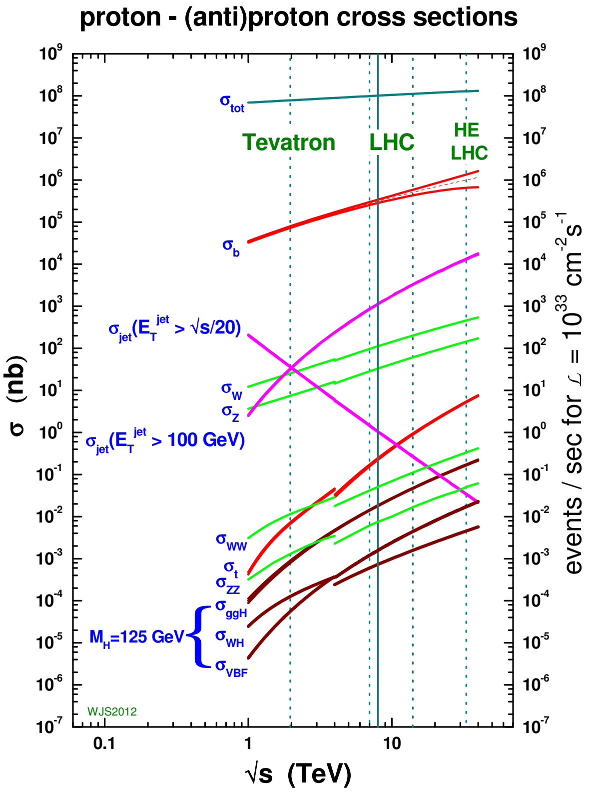

Figure 3.2: SM cross sections of proton-proton collisions as a function of center of mass energy with markers for existing and future upgraded hadron colliders [26].

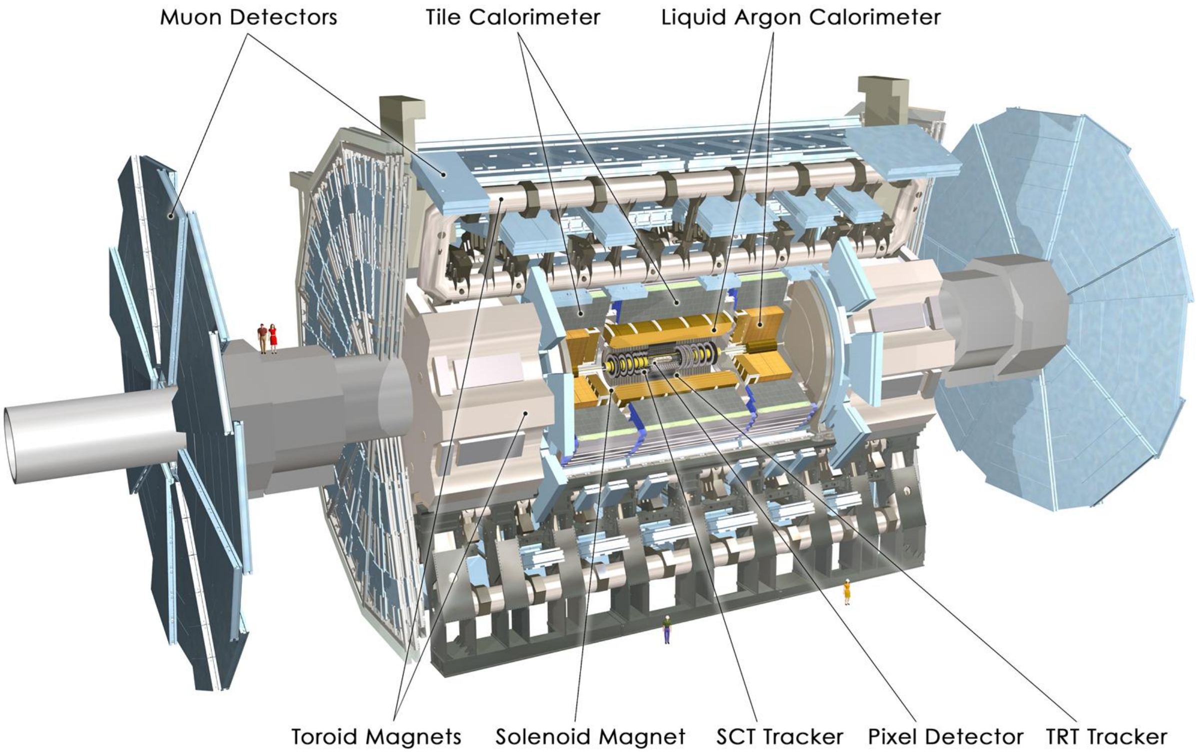

Figure 3.3: Computer-generated image of the whole ATLAS detectors showing major components [28]

3.2 The ATLAS Detector

The ATLAS Detector [27] is designed as a particle detector for hadron collisions and located underground in a cavern at Interaction Point 1 of the LHC. It aims to measure proton-proton collisions as comprehensively as possible, both in terms of coverage of the solid angle and in terms of capturing all final state particles and their kinematics, so that ATLAS can be used in a wide array of particle physics analyses.

ATLAS has the shape of a cylinder along the beam pipe, surrounding the interaction point (see figure 3.3) with a diameter of 25 m and a length of 46 m. The central parts of the detector, where components are mostly aligned concentrically around the beam pipe, are called the barrel, while the disk-shaped parts to both ends of the cylinder are called the endcaps. It consists of a number of subdetectors layered around the interaction point in the center. Superconducting magnets provide magnetic fields curving the paths of charged particles. Data recorded from the subdetectors can then be used to identify particles or to *track* them, i.e. reconstruct their trajectories, and to measure their momentum and energy.

3.2.1 Coordinate System

The coordinate system used at ATLAS defines the center of the detector and nominal interaction point as the origin. The x-axis points from the origin inwards towards the center of the LHC ring, the y-axis upwards towards the Earth's surface, and the z-axis along the beam axis, in such a way that the resulting coordinate system is right-handed.

From this carthesian coordinate system, cylindrical coordinates are derived and used in the x-y plane, transverse to the z-axis. The azimuthal angle ϕ is measured transverse plane, with $\phi = 0$ pointing to the x-axis, while the spherical angle θ is measured relative to the z-axis.

Quantities that only include contributions in this transverse plane are called transverse quantities, such as the transverse momentum p_{T}.

The angle θ is used to define the pseudorapidity η for convenience as

$$\eta = -\ln \tan \frac{\theta}{2} \tag{3.2}$$

The coverage of each subdetector is given in ranges of $|\eta|$, where $\eta = 0$ is the transverse plane and $\eta = \pm\infty$ is parallel to the beam pipe. High values of η are called the forward region.

3.2.2 Magnet System

The ATLAS detector has a system of superconducting magnets [29] integrated into it. It consists of the central solenoid magnet around the inner detectors and toroid magnets around the muon spectrometer, both located in the barrel region and the endcaps. Since moving charged particles are deflected in magnetic fields by the Lorentz force, the tracks in the detector are bent from a straight path. The angular deflection is proportional to the momentum of the particle, and the sign of its charge determines its direction of the deflection. Thus momentum and charge can be measured.

The relative resolution of a momentum measurement done using this method is proportional to the momentum and inverse proportional to the magnetic field [30]. So in order to keep the resolution small enough when dealing with particle energies produced at LHC collisions, the magnetic fields have to be so strong to compensate that only superconducting magnets can provide them.

3.2.3 Inner Detector

The inner detector (ID) [27] of ATLAS as illustrated in figure 3.4 has a cylindrical shape and is the closest subdetector to the interaction point. It starts only 3 cm from the beam axis and has an outer radius of 115 cm. The 2 T magnetic field from the solenoid magnet permeates the ID. Its purpose is to track and identify charged particles coming from the interaction point, and determine primary and secondary vertices, all with high spatial and momentum resolution.

The ID consists of three subdetectors, with the most precise one nearest the center, and covers a pseudorapidity region of $|\eta| < 2.5$. These are, starting from the center, the pixel detector, the semiconductor tracker (shown in figure 3.5), and the transition radiation tracker.

Pixel Detector The pixel detector consists of four layers of silicone pixel sensors arrayed around the beam axis at about 3 cm, 5 cm, 9 cm and 12 cm. The innermost layer, called the inner B-layer, has been inserted as an upgrade in expectation of the increase of luminosity what came along with the increase in center of mass energy from $\sqrt{s} = 8$ TeV to the current $\sqrt{s} = 13$ TeV after Run 1. There are also three disks of of sensors each along the z-axis in the transverse plane covering high values of $|\eta|$.

It works as two dimensional grid of p-n junctions between two reverse biased electrodes. A charged particle transversing the junction creates electron-hole pairs which are detected by the readout electronics.

An important task of the pixel detector is the reconstruction of secondary vertices, which are crucial in the tagging of jets containing b-hadrons.

Semiconductor Tracker The semiconductor tracker (SCT) is based on the same technology as the pixel detector. The SCT completely surrounds the pixel detector. Unlike the pixel detector it uses strips instead of pixels, reducing the number of output channels and the overall cost. It consists of four layers around the barrel at distances between 30 cm and 51 cm and nine disks on each endcap at distances from the interaction point between 85 cm and 273 cm. To obtain a second hit coordinate from the strips, alternating pairs of layers are rotated slightly with respect to each other.

Transition Radiation Tracker The Transition Radiation Tracker (TRT) [31] is the outermost subdetector of the ID. It consists of thin-walled drift tubes of 4 mm diameter layered around the SCT barrel and endcaps, such that typically particles cross between 35 and 40 tubes. Charged particles that cross materials with different index of refraction emit transition radiation in the form of photons in the TRT. These photons ionize the gas inside the tubes. Since this radiation is sensitive to the energy to mass ratio of the emitting particles, this aids in the identification of them, e.g. distinguishing between electrons and pions.

3.2.4 Electromagnetic Calorimeter

The electromagnetic calorimeter (ECAL) [33] encloses the inner detector in the barrel region and both endcaps as seen in figure 3.7. Its purpose is to measure the energy of electromagnetically interacting particles. The ECAL is a finely segmented sampling calorimeter with accordion-shaped lead and copper absorbers, and liquid argon (LAr) as the active material in between as shown in figure 3.6

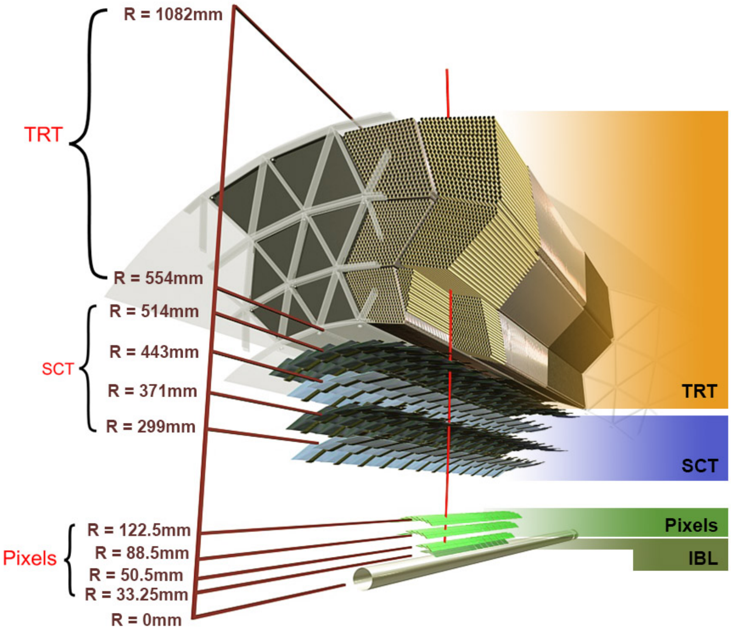

Figure 3.4: Computer-generated illustration of the ATLAS inner detector [32]

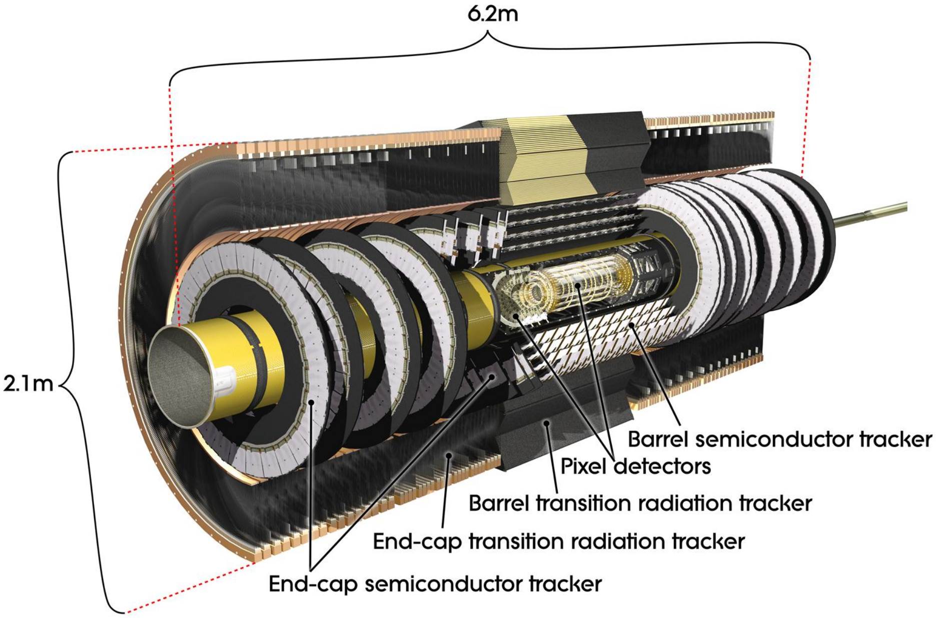

Figure 3.5: Silicon Tracker, consisting of pixel detector and semiconductor tracker [32]

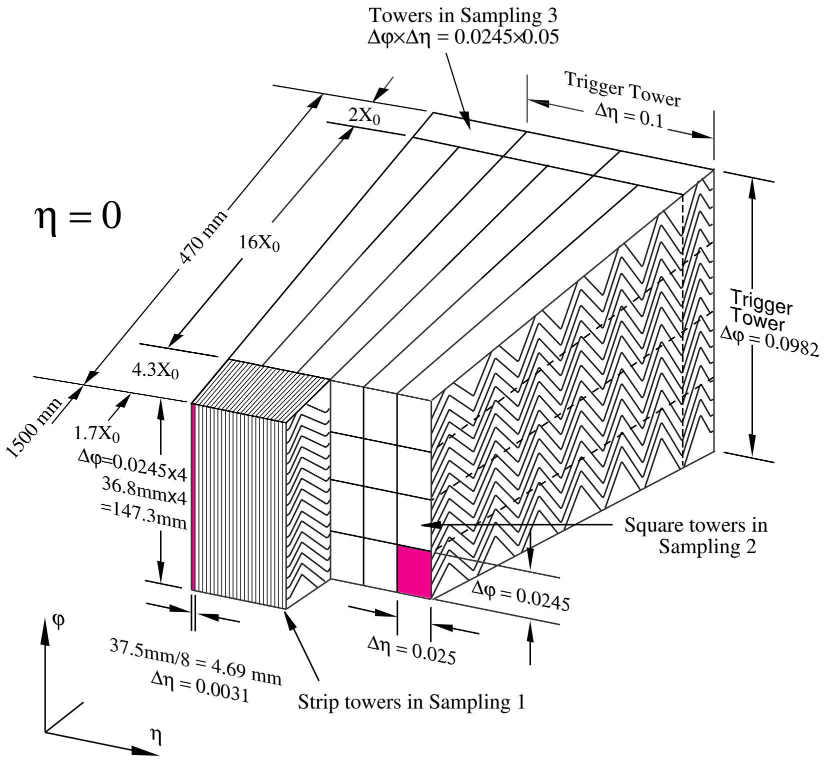

Figure 3.6: Schematic of the electromagnetic calorimeter with its distinctive accordion structure. [33]

An incoming particle interacts via the electromagnetic interaction with the absorber material, creating a shower of low energy particle, such as photons, electrons and positrons.

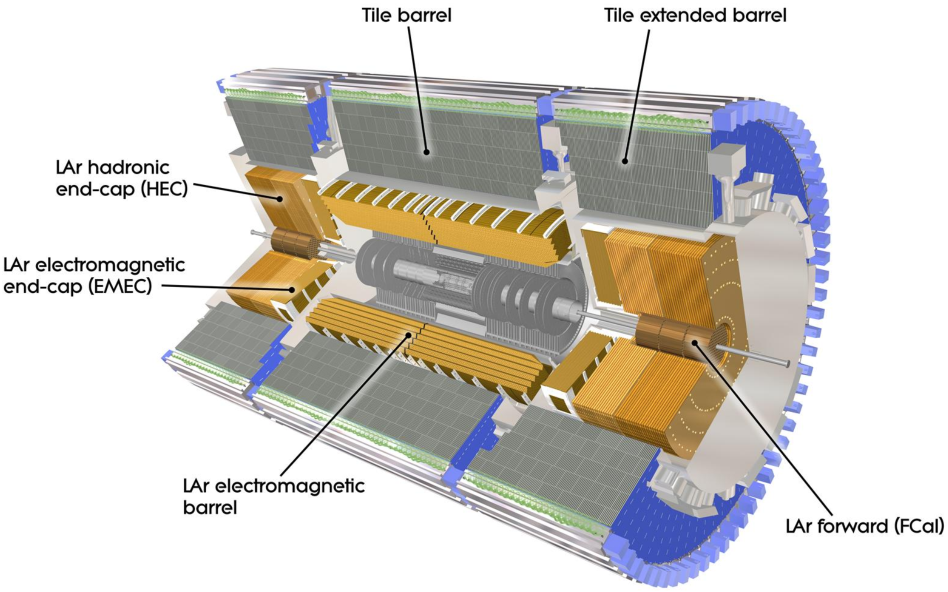

Figure 3.7: The ATLAS calorimeter system consisting of electromagnetic calorimeter and hadronic calorimeter. [34]

These in turn ionize argon atoms in the active areas of the calorimeter. Electric fields from high voltage cause the free electrons to drift to readout electrodes where they are measured. From the hits in the individual calorimeter cells, position and energy of the incoming particle as well as the shape of the shower can be determined.

3.2.5 Hadronic Calorimeter

The hadronic calorimeter (HCAL) surrounds the ECAL. Analogous to the ECAL, it is used to measure the energy of hadrons, such as protons, neutrons or π-mesons, which interact via the strong force. As seen in figure 3.7, the endcaps in a region of $1.5|\eta| < 3.2$ and in forward direction $3.1 < |\eta| < 4.9$ LAr calorimeters similar to the ECAL, but with copper and tungsten absorbers, are used for this purpose.

The tile calorimeter is installed in the barrel region of $|\eta| < 1.7$. It consists of steel absorbers alternating with scintillating tiles forming a sampling calorimeter. Incoming hadrons interact with the nuclei of the absorber material produce particles showers, which then excite the scintillator to emit photons. This light is then transported via wavelength shifting fibers to photomultipliers and subsequently measured.

3.2.6 Muon Spectrometer

The outermost subdetector of ATLAS is the muon spectrometer (MS) [35]. It is designed to both trigger on muons and measure their tracks and momenta with high accuracy. Its goal is to be able to reach a p_{T}-resolution of 10% for tracks at 1 TeV.

Muons are the only charged particles that usually penetrate all the inner layers of ATLAS and reach the MS. They have a lifetime of about 2.2 µs, long enough that most of them do not naturally decay before reaching the MS. As minimally ionizing particles at the energy scale present in ATLAS they lose little energy in the ID and calorimeters, and also do not participate in strong interactions.

The muon spectrometer as a whole sits inside the magnetic field from the toroid magnets and consists of four types of muon detectors. The magnetic field is largely oriented perpendicularly to the flight path of the muons in order to maximize deflection and thus resolution. A schematic view of the MS is shown in figure 3.8, once viewed in beam-direction and once from the side.

In the barrel region, three layers of monitored drift tubes (MDT) and resistive plate chambers (RPC) surround the beam axis at a distance of about 5 m, 7.5 m, and 10 m. On both endcaps, MDTs and thin gap chambers (TGC) are arranged in wheel shapes at distances of 7.4 m, 10.8 m, 14 m, and 21.5 m from the interaction point. In the forward region of $2 < |\eta| < 2.7$ Cathode-Strip Chambers (CSC) are installed on the innermost wheel.

Monitored Drift Tubes The MDT subdetector covers the pseudorapidity range of $|\eta| < 2.7$. It consists of three to eight layers of drift tubes, varying in length between 70 cm and 630 cm. Those are aluminium tubes with a diameter of 30 mm and a thickness of 400 µm with a central wire, which is held at high voltage. It is filled with an Argon-CO_2 mixture at a pressure of 3 bar. Passing muons ionize this gas, creating some ion-electron pairs. The electrons drift toward the central wire and create an electron avalanche, which is then measured.

Cathode-Strip Chambers CSC instead of MDT are used in the forward region near the interaction point because they are capable of handling the higher particle rates in that region. They are multiwire proportional chambers, oriented such that the wires point radially outward. Both of the chamber cathodes are segmented, one parallel and the other perpendicular to the wires, so the CSC can provide two-dimensional positional information.

Resistive Plate Chambers Three layers of RPC are used in the barrel region for triggering. They consist of two charged parallel plates with a gas-filled gap of 2 mm and no wires in between. The signal readout is segmented into strips, which are coupled capacitively to the plates. The small size of the RPC allow for a time resolution of less than 2 ns, which makes them usable as triggers.

Thin Gap Chambers The TGC installed in the endcaps are also used to trigger. They, too, provide the measurement of a second coordinate, perpendicular to the MDT in the endcaps. They work, similar to the CSC, as multiwire proportional chambers and because of their compactness they are fast enough be be used in triggers.

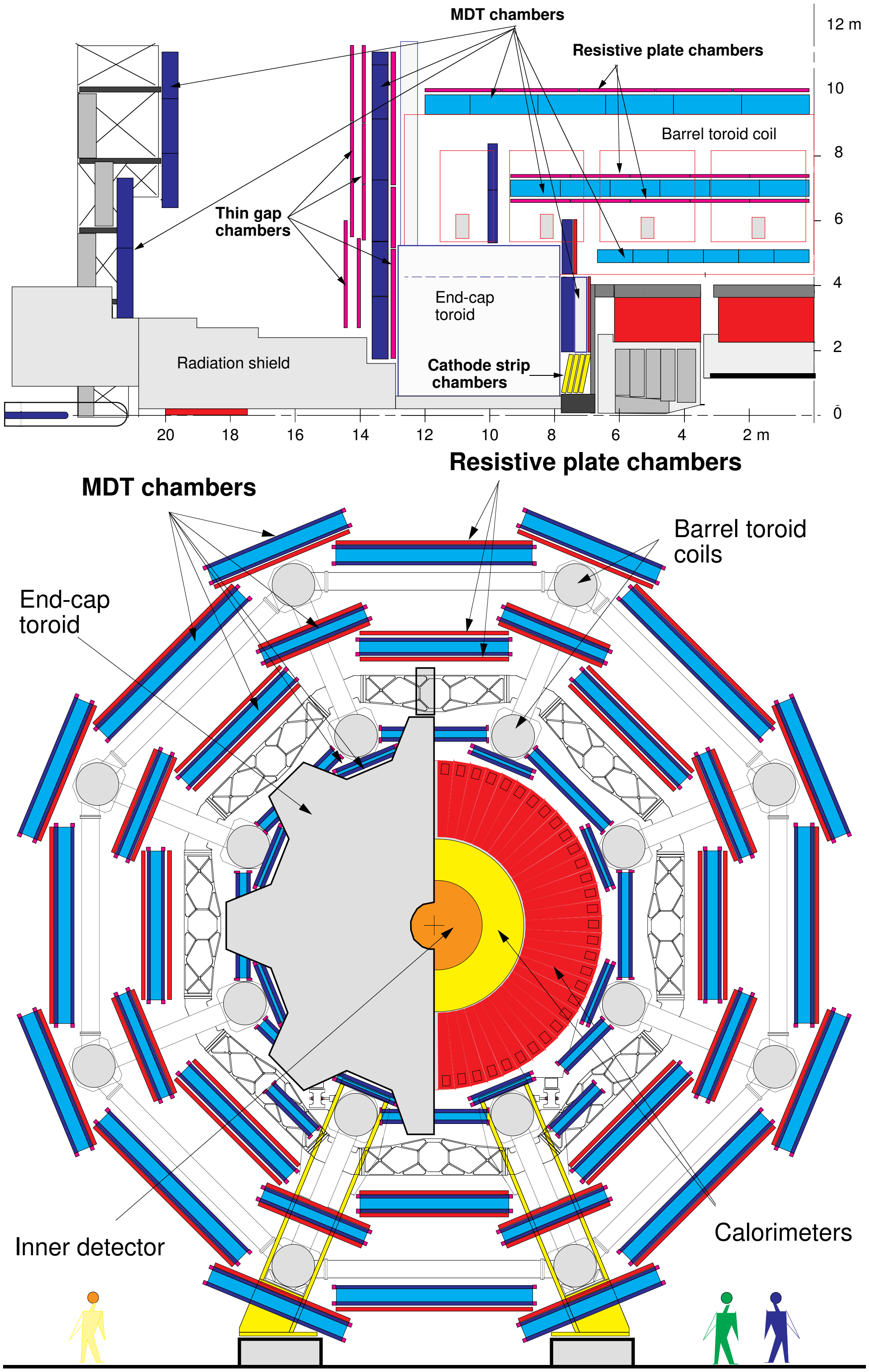

Figure 3.8: Side view of one quadrant (top) and transverse view (bottom) of the ATLAS muon spectrometer [35]. Human figures for scale.

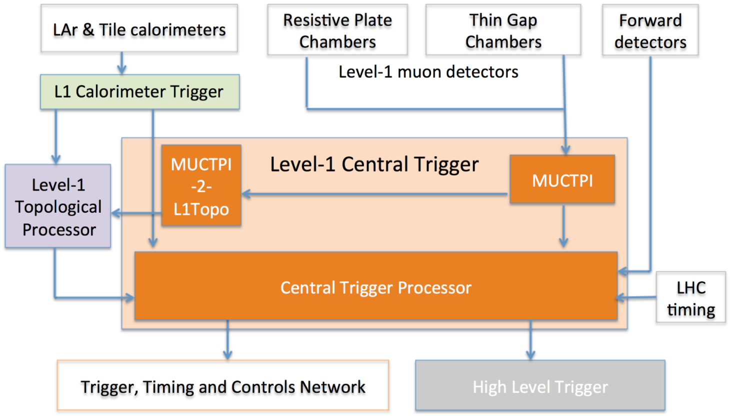

Figure 3.9: Schematic overview of the Level 1 trigger system [37]

3.3 Trigger and Data Acquisition

During the data taking in 2015 the proton bunches collided at a rate of about 40 million per second inside the ATLAS detector. In each bunch crossing, an average of 13.7 proton-proton interactions occurred. The recording of one bunch crossing, called an event, produces about 1.5Mb of data. It is not technically feasible to record such a tremendous stream of data into permanent storage. To reduce the amount of data, the ATLAS trigger system [36] is used. It is a two step filtering process, that picks out events that are of interest for the various physics analyses and discards the rest.

The first step is the Level-1 (L1) trigger [37] implemented in custom build hardware. An overview of its central components is shown in figure 3.9. It reduces the event rate from the bunch crossing rate down to approximately 100 kHz, making a decision whether to keep an event or not in 2.5 µs. To that end it analyses coarse granularity data from parts of the calorimeters and the muon spectrometer and determins regions of interest (RoI).

If the L1 trigger found RoIs, they are sent to the high level trigger (HLT). The HLT consists of sophisticated software running in a large farm of conventional servers. It has access to the fully granular detector information and makes a decision either on data from the RoI alone or if needed from the whole event. or if needed the whole event. It can perform a preliminary reconstruction of the event. The HLT reduces the event rate down again to an output rate of about 1 kHz. The selected events are then fully read out of the detector and written into permanent storage at a local computing center at CERN.

3.4 Grid Computing

The amount of data produced by ATLAS and the other experiments at CERN is so large, that it is unfeasible to analyze it all directly at CERN. To handle the computational requirements, the Worldwide LHC Computing Grid has been created. It consists of more than 170 computing centers in 42 countries, provided by entities like universities and other

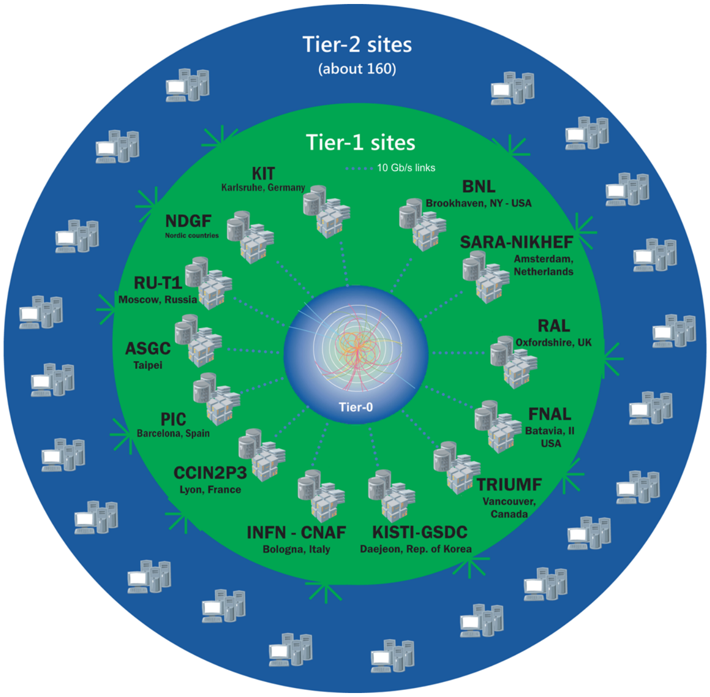

Figure 3.10: The tier structure of the Worldwide LHC computing Grid [38]

scientific research institutions.

The grid is organized hierarchically in tiers [38] as illustrated in figure 3.10. Tier-0 is the entry point for all ATLAS data. It consists of a data center locally at CERN in Geneva and at the Wigner Research Centre for Physics in Budapest, both connected to each other via two dedicated 100 Gbit data links. At Tier-0, all raw data are stored permanently, some first reconstruction is performed and copies of raw and reconstructed data are from there redistributed into Tier-1.

Tier-1 is made up of thirteen large computing centers of sufficient capacity in terms of storage, computing power and data transmission bandwidth. Associated to each Tier-1 center is a “cloud” of Tier-2 centers, with a total number of about 160. They typically handle generating and reconstructing simulated events, as well as analyzing reconstructed data at a large scale. Local workstations and personal computers of scientists who access the grid infrastructure are referred to as Tier-3.

Working groups and individual analyzers can submit requests into the grid to perform tasks for them, such as retrieving certain datasets and running analysis software on specified inputs. Sophisticated software systems like PanDA[1] and Rucio [39] handle the correct scheduling, execution and monitoring of individual subtasks in the grid as well as the distribution and management of datasets. The grid allows for distributed analysis on thousands of computer simultaneously and thus makes it possible to cope with the tremendous demands on computing resources of modern particle physics experiments.

---

[1] Production and Distributed Analysis system

Chapter 4

Higgs Boson Production and Decay at the LHC

4.1 Higgs Production Processes

At the LHC Higgs bosons can be produced by a number of different mechanisms. The cross sections of these processes generally decrease with increasing mass of the Higgs boson m_{H}, as shown for the dominant processes in figure 4.1. However they increase with the center of mass energy of the proton proton collision, shown in figure 4.2.

In gluon-gluon fusion (ggF) two gluons in the initial state combine over a quark loop into a Higgs boson. Since the Higgs-fermion coupling increases with the fermion mass, this loop is dominated by virtual top quarks, followed by bottom quarks.

Higgs bosons can also be created in Vector-Boson Fusion (VBF). Here two initial state quarks, one from each incoming proton, both radiate a W or Z boson, which then fuse into a Higgs boson. In this process the quarks are each deflected to some degree from the beam, which leads to two jets which are roughly opposite in the detector and near the z-axis.

Another process is the vector boson associated production (VH), sometimes called Higgsstrahlung. In this case initial state quarks annihilate into a W or Z vector boson, which then radiates off a Higgs boson.

Also top quark fusion (ttH) can occur, where two gluons from the initial state each produce a top-antitop pair. One top and one antitop quark from each pair then fuse into a Higgs boson, while two other ones become part of the final state. This can also happen with other quark flavors. However, since the coupling to the Higgs boson decreases with decreasing quark mass, the resulting cross sections are negligible.

4.2 Higgs Boson Decay

After their production, Higgs bosons decay into a number of possible final states, each with an associated probability called branching ratio or branching fraction. Figure 4.3 shows

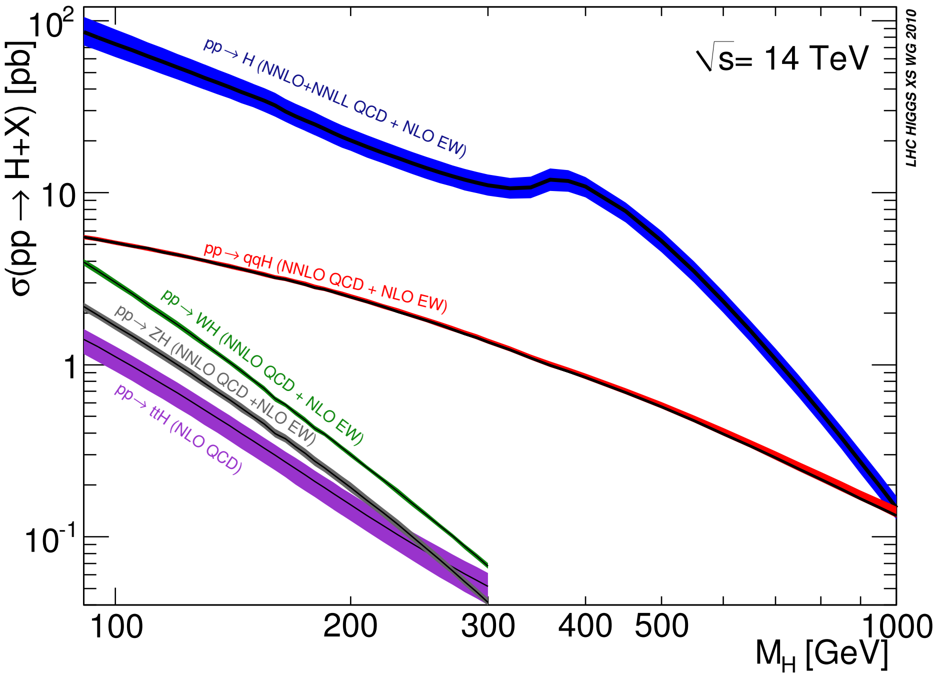

Figure 4.1: Standard Model Higgs boson production cross sections at center of mass energy $\sqrt{s} = 14\,\mathrm{TeV}$ as a function of the Higgs mass m_H for $m_\mathrm{H} = 125\,\mathrm{GeV}$ [40]. ggF in blue dominates, followed by VBF in red, the VH processes with W (green) and Z bosons, and lastly ttH in purple. The colored bands represent one standard deviation of theoretical uncertainty.

the prediction of these branching ratios for the dominant decays as a function of the mass of the Higgs boson.

The natural decay width of the Higgs boson as seen in figure 4.4 is very small. For a Higgs masses $m_\mathrm{H} < 200\,\mathrm{GeV}$ it is on the sub-GeV level. Hence the natural width is negligible compared to the detector resolution, which is on the order of several GeV.

One of the predicted Higgs boson decays is the decay into muon-antimuon pairs. Here a Higgs boson decays directly, i.e. without any intermediate particles, into a muon-antimuon pairs, by the vertex depicted in figure 4.5. The prediction of the branching ratio of the $\mathrm{H} \to \mu\mu$ decay varies from $2.8 \cdot 10^{-4}$ and $6.5 \cdot 10^{-5}$ [41] in the studies range of Higgs masses m_H between 110 GeV and 150 GeV.

4.3 The $\mathrm{H} \to \mu\mu$ Signal

The goal of this analysis is to probe the direct coupling between the Higgs boson and muons. At the LHC, this is only possible via the direct decay of Higgs bosons into muon-antimuon pairs. Hence this analysis is looking for such events, in which this $\mathrm{H} \to \mu\mu$ decay occurs. Of the number of Higgs production processes that are possible at the LHC, only

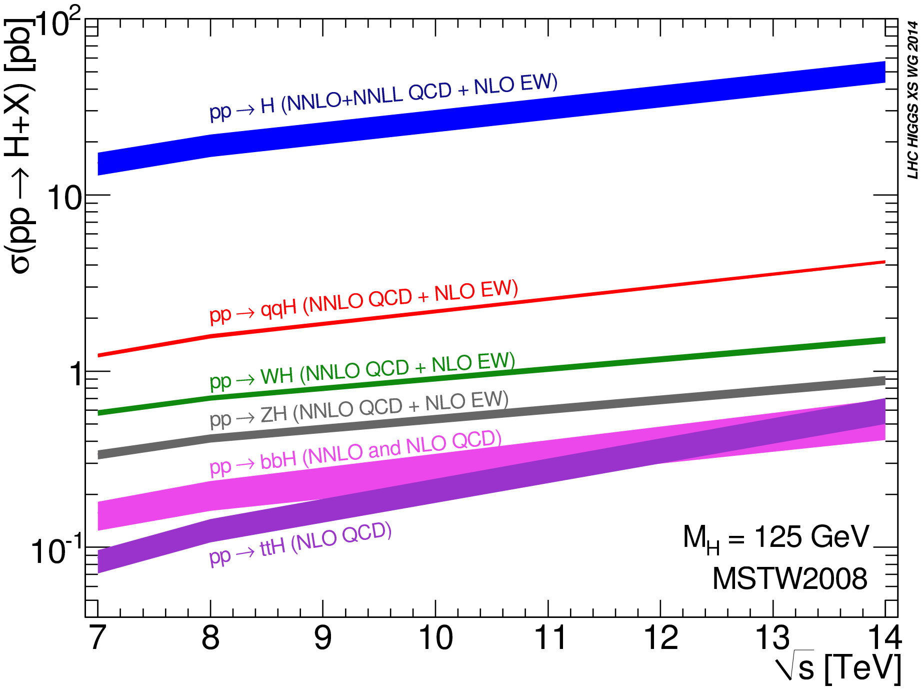

Figure 4.2: Standard Model Higgs boson production cross sections at center of mass energy $\sqrt{s} = 14\,\mathrm{TeV}$ as a function on $\sqrt{s}$ for $m_\mathrm{H} = 125\,\mathrm{GeV}$ [40] for the processes ggH (blue), VBF (red), VH with W (green) and Z bosons, and ttH (purple). The colored bands represent one standard deviation of theoretical uncertainty.

the following two are non-negligible.

The two signal processes as used in this analysis are then defined by the Higgs production process combined with a H → $\mu\mu$ decay. Those are the gluon gluon fusion and vector boson fusion, both of which leave related but different signatures in the detector. Both signals have in common exactly one muon and one antimuon in each event, whose combined invariant mass corresponds to the mass of the Higgs boson. This combined di-muon system also exhibits high transverse momentum $p_\mathrm{T}^{\mu\mu}$.

4.3.1 Gluon Gluon Fusion

The dominant signal process is gluon gluon fusion (ggF). This is mainly due to the high proportion of gluons with the sufficient momentum fractions needed to produce Higgs bosons at the center of mass energy of the LHC in the incoming protons. Since gluons are massless and therefore do not couple directly to the Higgs field, the fusion is mediated by a fermion loop with contributions mostly from heavy fermions like top and bottom quarks, as shown in figure 4.6.

Apart from the muon-antimuon pair, there may be one or more jets in a ggF event stemming from additional gluons radiated from the gluons in the initial state.

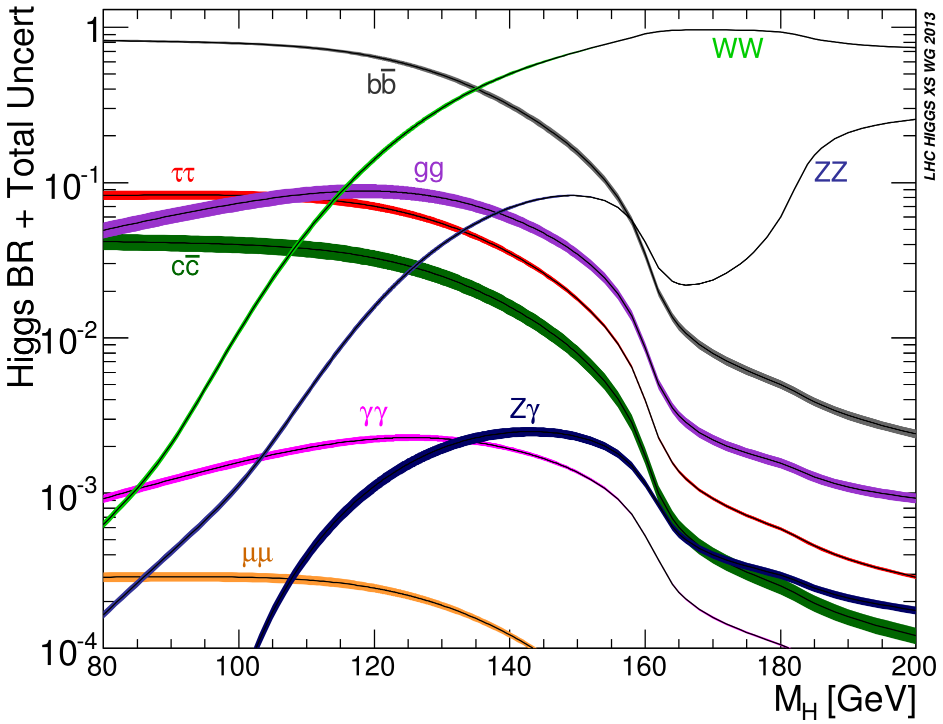

Figure 4.3: Standard Model Higgs boson decay branching ratios [41] for the dominant decays as a function of Higgs mass m_H The colored bands represent one standard deviation of uncertainty.

4.3.2 Vector Boson Fusion

The other signal channel is Vector Boson Fusion (VBF) as illustrated in figure 4.7. Here two quarks in the initial state both radiate either a W or Z boson each, which fuse into a Higgs boson. In contrast to ggF production, this leads to two additional high energy jets emerging in opposite direction from the collision point near the beam axis. Selecting events with these two jets and their specific kinematic signature can be exploited to suppress background.

4.3.3 Other Production Mechanisms

Other production mechanisms like production in association with vector bosons or heavy quarks as depicted in figure 4.8 are not included in this analysis. Their small cross sections combined with the small H $\rightarrow \mu\mu$ branching ratio leads a very small number of expected events. would only be relevant, if they happened often enough to yield a sufficient number of events. Including the small branching fractions of H $\rightarrow \mu\mu$, those channels are predicted to yield much less than one event in the whole studied dataset, and are therefore negligible and are not included in the further analysis.

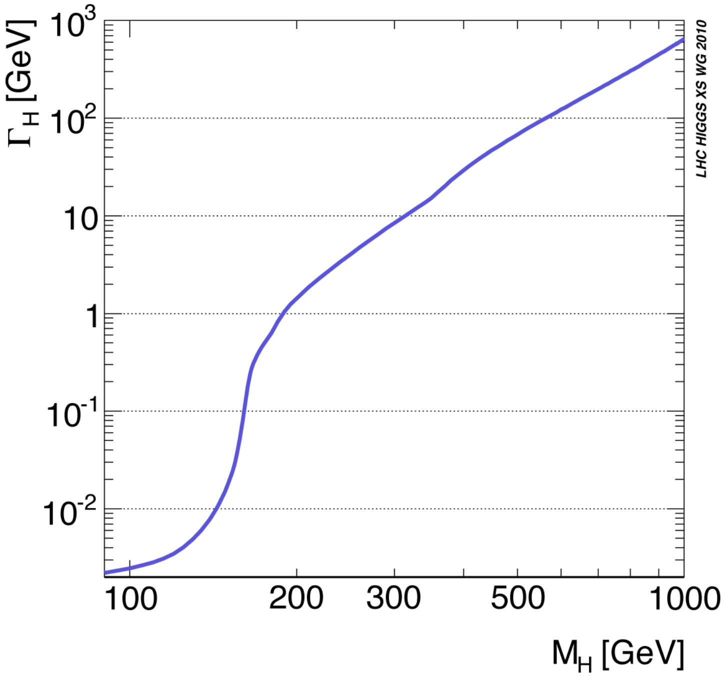

Figure 4.4: Predicted natural width of the Standard Model Higgs boson depending on its mass m_{H}

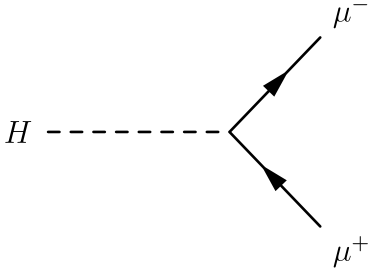

Figure 4.5: The direct decay of a Higgs boson into a di-muon pair

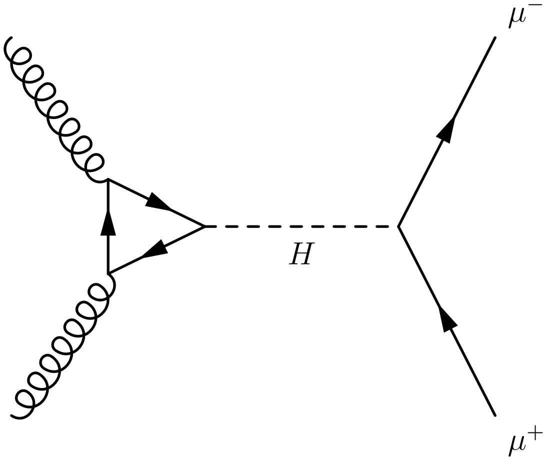

Figure 4.6: Feynman graph of the ggF signal. Two initial state gluons form a Higgs boson via a fermion loop. The Higgs boson subsequently decays into a muon-antimuon pair.

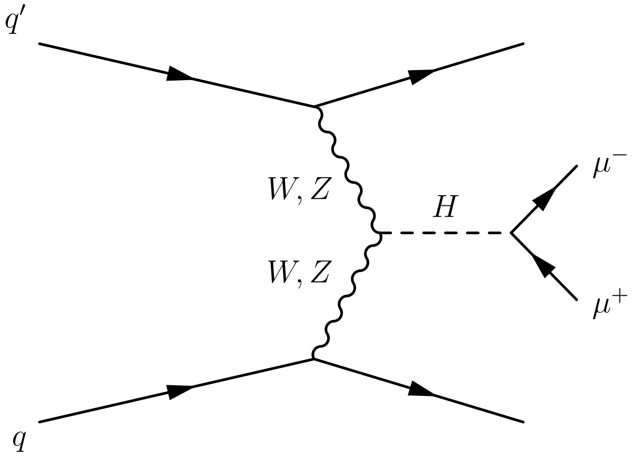

Figure 4.7: Feynman graph of the VBF signal. Two weak bosons, emitted from initial state quark form a Higgs boson, which subsequently decays into a muon-antimuon pair.

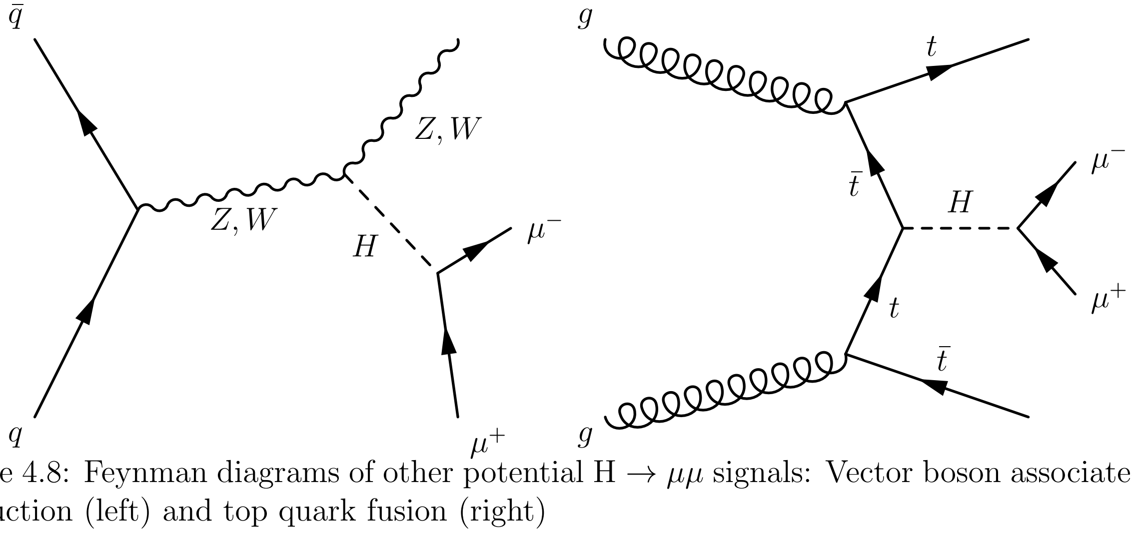

Figure 4.8: Feynman diagrams of other potential H → $\mu\mu$ signals: Vector boson associated production (left) and top quark fusion (right)

Chapter 5

Data and Monte Carlo Samples

5.1 Data taken with the ATLAS detector

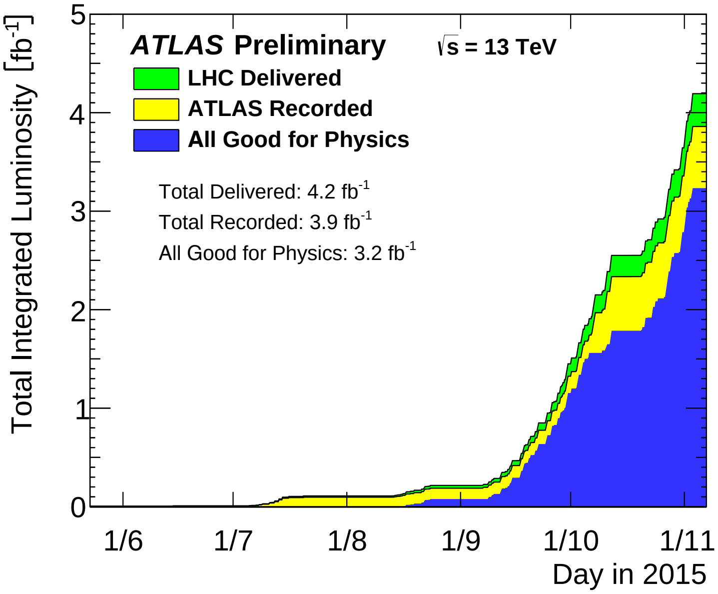

Figure 5.1: Integrated luminosity over time during the 2015 data taking at ATLAS

The dataset used in the H → $\mu\mu$ analysis was taken by ATLAS in 2015 at a center of mass energy of 13 TeV. Figure 5.1 shows the amount of integrated luminosity over time. Of the $\int dt \cdot \mathcal{L} = 4.2\,\text{fb}^{-1}$ that were delivered by the LHC machine, ATLAS managed to record $3.9\,\text{fb}^{-1}$. Of the recorded data, $3.2\,\text{fb}^{-1}$ were deemed all good for physics by the so called good run list (GRL). It specifies which blocks of luminosity fulfill certain quality criteria. During the time the corresponding data was taken, all relevant subdetectors of ATLAS have to be fully operational for a luminosity block to quality as good.

Not used in this analysis was a data taking period with very little corresponding inte-

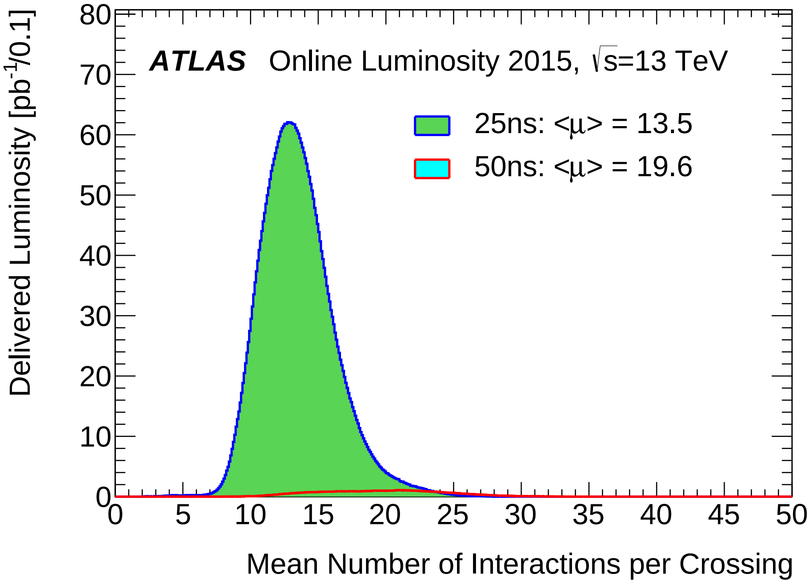

Figure 5.2: Mean number of proton-proton interactions $< \mu >$ per bunch crossing for the 25 ns and 50 ns data taking periods in 2015. The small contribution of 50 ns data in light blue is not used in this analysis.

grated luminosity early in 2015, when the bunch spacing was set to 50 ns. In the rest of 2015, which was used, it was set to 25 ns. In this period, the mean number of proton-proton collisions per bunch crossing was $< \mu >= 13.5$, as seen in figure 5.2.

5.2 Monte Carlo samples

Signal samples have been generated for Higgs masses between 100 GeV and 150 GeV in steps of 5 GeV using Powheg-Box v2 [42] at next-to-leading order (NLO) using the CT10 [43] parton distribution function (PDF) set. Parton showering and hadronization has been simulated using Pythia 8.186 [44]. The spectrum of the Higgs boson p_T in gluon-gluon fusion has been tuned to agree with the prediction from Hres [45][46]. The cross sections of the Higgs production is taken from the CERN report 4 [47]. The ggF production cross section is calculated in next-to-next-to-next-to-leading order in QCD [48] and NLO in electroweak (EW) corrections [49]. For the VBF production cross sections include full NLO QCD and EW corrections [50][51][52] and approximate NNLO QCD corections [53]. The H $\rightarrow \mu\mu$ branching ratios have been calculated using Hdecay [54].

For dominant Drell-Yan background two alternative samples are used. One has been generated using MadGraph5 [55] with NNPDF23LO PDF [56] and one with Powheg-Box v2, both interfaced with Pythia 8.186. Top-pair and single top production has been generated with Powheg-Box v2 using CT10 PDF interfaced to Pythia 6.428 [57] with the top mass set to 172.5 GeV. The processes with two vector bosons (WW, WZ and ZZ) have been generated with Sherpa v2.1.1 [58] using the CT10 PDF set. For all Monte Carlo samples the detector response of ATLAS has been fully simulated [59] in a detector simulation of ATLAS based on Geant4 [60].

Chapter 6

Trigger and Event Selection

6.1 Trigger

In order to obtain the highest possible number of events, this analysis uses the trigger with the lowest muon p_{T} threshold ATLAS can offer that is not prescaled, i.e. all events passing this trigger are actually recorded. It requires a muon with at least $p_{\mathrm{T}} > 15\,\mathrm{GeV}$ in the L1 trigger and a isolated muon with $p_{\mathrm{T}} > 20\,\mathrm{GeV}$ in the HLT. Events passing this trigger (HLT_mu20_iloose_L1MU15) are the starting point of the event selection.

6.2 Primary Vertex and Pileup

Vertices are points in space in the detector where an interaction has taken place. A vertex is reconstructed from tracks in the inner detector [61]. The *primary vertex* is taken to be the vertex with the highest sum of transverse momenta of the tracks associated with it. It also has to have at least two tracks originating from it with a $p_{\mathrm{T}} > 400\,\mathrm{MeV}$ each. It is taken as the point of the hard interaction, and all impact parameters are calculated with respect to this primary vertex.

In one bunch crossing, typically more than one proton-proton interaction occurs. Each of them can give rise to multiple reconstructed vertices. The presence of interactions beside the one interaction, for which an event has been selected, is called pileup. The rate of proton-proton interactions is dependent on the instantaneous luminosity while data taking, so its distribution is not known a priori. This means, the MC has be re-weighted from a rough estimate of the predicted distribution to the actual distribution as measured in the data in a process called pileup re-weighting. To improve the agreement in the number of proton-proton interactions N_{int} and the agreement in the number of primary vertices between data and MC, N_{int} is rescaled in data by a factor of $^{1}/_{1.16}$ before applying the pileup re-weighting.

6.3 Object Definition

Objects in the context of a particle detector are the output of reconstruction algorithms applied to to raw data measured in the detector. They describe the final state of a particle interaction in terms of final particles like muons, collections of particles that travel in the same direction called jets and missing transverse energy, an abstract object introduced to balance overall momentum.

6.3.1 Muons

The muons used in this analysis are reconstructed from hits both in the ID and the MS [62]. In each subdetector, the track is reconstructed separately, and in a second step a s- called combined muon [63] is formed if they can be successfully combined into a single track. Therefore hits from both ID and MS are fitted together in one global fit, where hits from the MS can be added or removed to improve fit quality. Most muons that are reconstructed this way start from the MS track and are extrapolated to appropriate ID hits, but also the reverse procedure, i.e starting from a reconstructed ID muon, is used.

To be selected, muons have to originate from the primary vertex as described in section 6.2. This is why they are required to have a transverse impact parameter d_0, measured with respect to the beam line, of no more than three times the significance of that very measurement ($\frac{|d_0|}{\sigma_{d_0}} < 3$). In addition, there is a requirement on the longitudinal impact parameter z_0 and the angle θ of the muon track such that $|z_0 \cdot \sin\theta| < 5\,\mathrm{mm}$.

A set of quality cuts on the quality in the inner detector are applied to pass the so-called *medium* [64] criterion, ...

In order to distinguish muons coming from the signal process from those originating from various QCD backgrounds and decays, the amount of activity near each muon is considered. Signal muons are typically isolated, i.e. with low nearby activity in the detector. The discriminating variable is the ratio of $p_{\mathrm{T}}^{\mathrm{varcone30}}$ to the transverse momentum of the muon, where $p_{\mathrm{T}}^{\mathrm{varcone30}}$ is the scalar sum of the transverse momenta of all tracks with $p_{\mathrm{T}} > 1\,\mathrm{GeV}$ inside a cone with radius $\Delta R = \min(10\,\mathrm{GeV}/p_{\mathrm{T}}^{\mu}, 0.3)$. The cone size is chosen to be p_{T}^{μ}-dependent to improve performance for high energy muons.

A cut, which depends on η^{μ} and p_{T}^{μ}, on this relative isolation is applied such that the efficiency of selecting muons is a constant 99 % for all values of η^{μ} and p_{T}^{μ}. This corresponds to *LooseTrackOnly* working point for muon isolation as defined by the ATLAS Collaboration.

Selected muons are also required to have a transverse momentum of more than 15 GeV and an absolute pseudorapidity $|\eta| < 2.5$.

6.3.2 Jets

Hadronic jets are reconstructed from clusters of energy deposited in the calorimeter using the anti-k_t algorithm [65].

The radius parameter R of the algorithm is set to 0.4. Jets are rejected if they fail a number of standard quality requirements [66], designed to reject fake jets from background processes. The transverse momentum of the reconstructed jets are required to exceed 25 GeV and have $|\eta| < 2.4$, or to exceed 30 GeV and have $|\eta| < 4.5$. In addition, jets with $p_T < 50\,\mathrm{GeV}$ and $|\eta| < 2.4$ are only accepted if their so-called Jet Vertex Tagging (JVT) variable [67] is greater than 0.64. The JVT technique is a multivariate method that aims to suppress pileup jets, and select jets originating from hard scattering events.

6.3.3 *b*-Jets

Jets which originate from hadrons containing b-quarks are called as b-jets. They are distinguished from light jets using b-tagging algorithms. These exploit the properties of b-hadrons, such as their relatively long live time and high mass, which lead to signatures distinguishing b-jets from light jets. Because of its long live time, a hadron containing a b-quark will travel a measurable distance from the primary vertex before decaying, resulting in a displaced secondary vertex. In the MV2c20 method [68] 24 input variables, the geometry and kinematics of the secondary vertex and associated jets are combined in a neural network. The algorithm is set to a working point of 85% detection efficiency of correctly identifying b-jets in simulated $t\bar{t}$ events [69].

6.3.4 Missing Transverse Energy

The momenta of the incoming partons in a proton-proton collision in ATLAS are almost entirely aligned in the z-direction. Therefore, conservation of momentum requires the total momentum of the outgoing particles in each collision to be zero in the plane transverse to the z-axis. The missing transverse momentum with magnitude E_{T}^{miss} is defined as the negative sum of the vectors of all selected reconstructed and calibrated muons, electrons and jets. It also includes tracks originating from the primary vertex, which are not associated with any of those physics objects. These so-called soft terms in the E_{T}^{miss} calculation are derived from ID tracks rather than calorimeter cells, which would also be a possibility.

High values of E_{T}^{miss} can be caused, barring measuring errors, by particles that cannot be measured by ATLAS, like neutrinos or other only weakly interacting particles.

6.3.5 Overlap Removal

The ATLAS detector reconstructs different physics objects by using specialized algorithms for each type of object (i.e. jets, electrons, etc.). But since these algorithms rely on shared information (i.e. tracks and clusters in the various subdetectors), one actual physics object may be reconstructed multiple times and as different types of objects. To avoid this kind of double counting, overlap removal is applied. This means removing one reconstructed object and keeping the second one, when two are too close to each other in the $\eta - \phi$ plane. A distance ΔR in this plane is defined as $\Delta R = \sqrt{\Delta\eta^2 + \Delta\phi^2}$.

Firstly, selected electrons which share a track in the ID with a selected muon are removed. Then jets, which lie inside a cone of $\Delta R < 0.2$ of a selected electron or within $\Delta R < 0.4$ of a selected muon are ignored. In the next step electrons that are within $\Delta R < 0.4$ of a selected jet are rejected. Lastly, all selected muons that overlap with selected jets with more than three ID tracks are removed.

6.4 Event Selection

Events are selected from the full dataset if they contain exactly two muons as described in section 6.3.1. The muon with the higher transverse momentum, the so-called leading muon, has to exceed 25 GeV, whereas the other muon, the so-called subleading muon, has to have at least 15 GeV. The resulting muon p_T distribution is shown in figure 6.3

Since the Higgs boson is neutral, the muon pair is required to have a total charge of 0, i.e. the two muons have to be of opposite charge. Furthermore the missing transverse energy as shown in figure 6.4 must be lower than 80 GeV, and the event must contain no *b*-jets as defined in section 6.3.3. The number of expected signal and background events, as well as measured events in data, for this selection are shown in the cutflow in table 6.1.

$\sqrt{s} = 13TeV$, $\mathcal{L} = 3.2091 fb^{-1}$, $\mu\mu$	VBF [125 GeV]	ggF [125 GeV]	Background	Data
Trigger Selection	1.60 ± 0.01	18.40 ± 0.08	2656843.00 ± 2167.56	2656843
IsoLooseTrackOnly Selection	1.57 ± 0.01	18.04 ± 0.08	2557119.00 ± 2136.80	2557119
$p_t^{lead} > 25$ GeV	1.57 ± 0.01	17.98 ± 0.08	2470509.00 ± 2107.05	2470509
$p_t^{sublead} > 15$ GeV	1.57 ± 0.01	17.98 ± 0.08	2470509.00 ± 2107.05	2470509
Opposite sign muons	1.57 ± 0.01	17.98 ± 0.08	2379059.07 ± 992.32	2468635
$100GeV < M_{\ell\ell} < 160$ GeV	1.54 ± 0.01	17.60 ± 0.08	100197.80 ± 199.13	100573
$E_T^{\mathrm{miss}} < 80$ GeV	1.53 ± 0.01	17.55 ± 0.08	98034.92 ± 198.76	98481
b-jet veto	1.37 ± 0.01	16.79 ± 0.07	92274.96 ± 195.25	91877

Table 6.1: Cutflow of the number expected VBF and ggF signal events, total background events and measured data events for each step in the eventselection.

Those selected events are then split up into seven signal regions with varying signal and background composition and shape. Treating the signal regions separately and in a final step combining the results in the statistical treatment improves the overall sensitivity over an inclusive approach.

One region is defined to include a high proportion of signal originating from Vector Boson Fusion and is designated the VBF region. It requires exactly two jets as described in section 6.3.2. They have to have a combined invariant mass $m_{jj} > 500\,\mathrm{GeV}$, be located in opposite hemispheres of the ATLAS detector, and have a difference in pseudorapidity $\Delta\eta_{jj} > 3$.

All selected events that are not accepted into the VBF region, are split up based on the transverse momentum of the di-muon system, $p_\mathrm{T}^{\mu\mu}$ as shown in figure 6.1. Events with $p_\mathrm{T}^{\mu\mu} < 15\,\mathrm{GeV}$ are marked as low-$p_\mathrm{T}^{\mu\mu}$. Those in the range $15\,\mathrm{GeV} < p_\mathrm{T}^{\mu\mu} < 50\,\mathrm{GeV}$ are marked as mid-$p_\mathrm{T}^{\mu\mu}$. The rest with $p_\mathrm{T}^{\mu\mu} > 50\,\mathrm{GeV}$ is marked as high-$p_\mathrm{T}^{\mu\mu}$.

In each of those $p_\mathrm{T}^{\mu\mu}$ ranges, the events are then finally categorized based on the pseudorapidity η_μ of the two muons. The pseudorapidity distributions of the leading and subleading muon is shown in figure 6.2. In order to be classified as central, the η_μ of both muons has to be smaller than 1. This is done to exploit the better than average muon momentum resolution in this region of the detector. All other muons are classified as non-central.

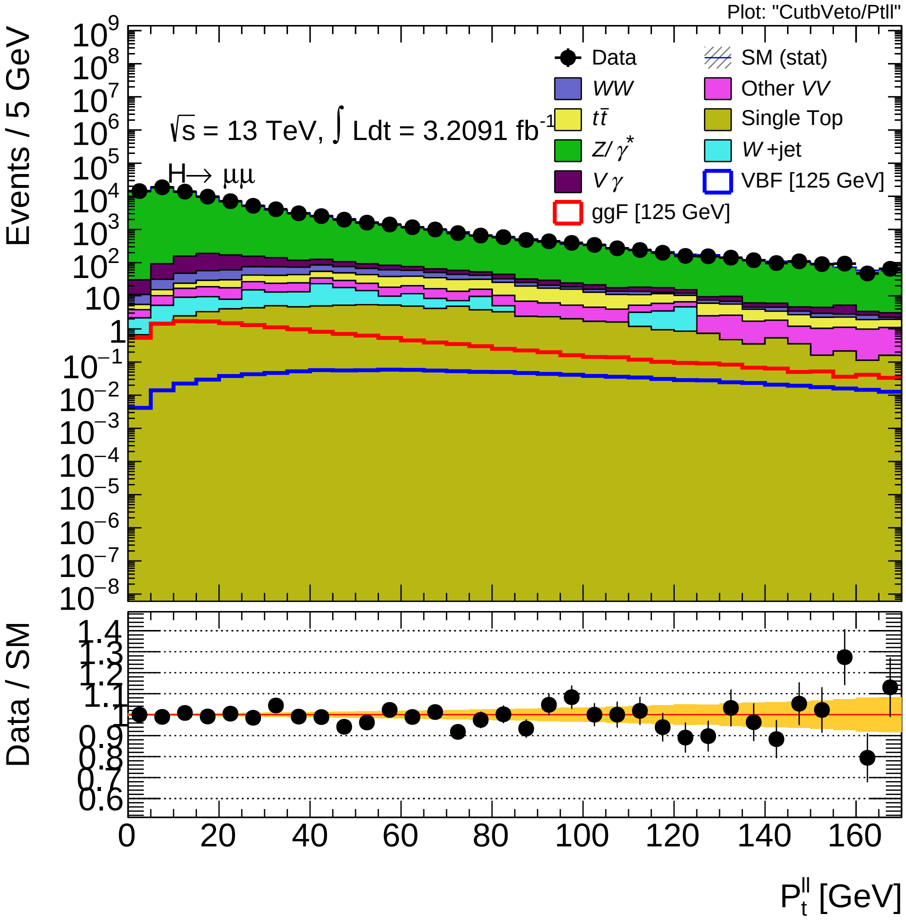

Figure 6.1: The transverse momentum of the di-muon system $p_{\mathrm{T}}^{\mu\mu}$. The signal is shown for $m_{\mathrm{H}} = 125\,\mathrm{GeV}$. In the lower part of the plot the ratio between the data and the background MC is shown, with the yellow band indicating the statistical uncertainty.

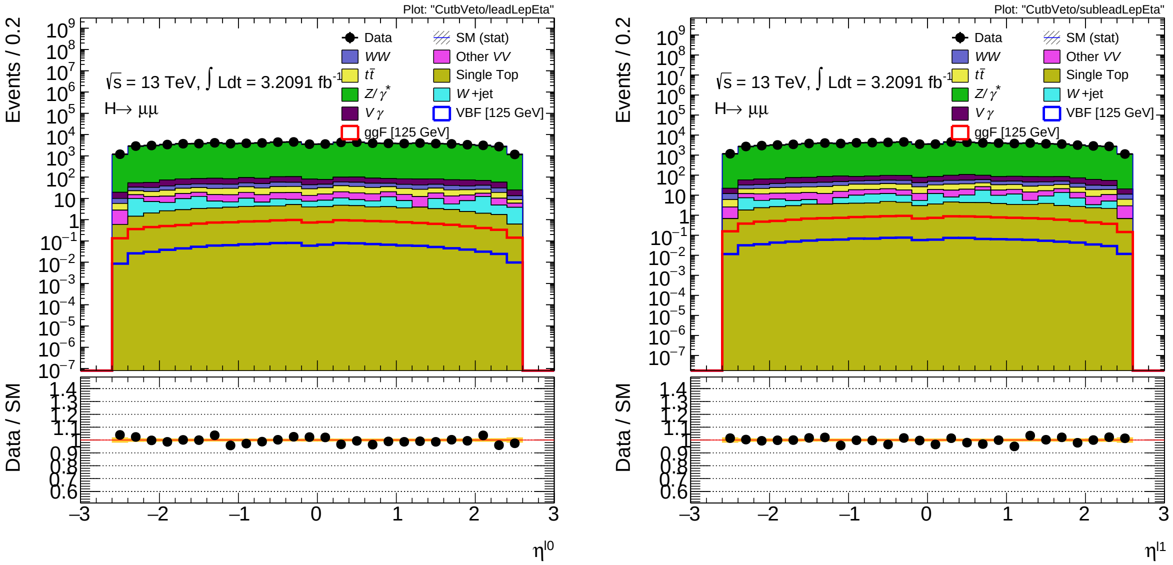

Figure 6.2: The pseudorapidity η of the leading (left) and subleading (right) muon. In the lower part of the plot the ratio between the data and the background MC is shown, with the yellow band indicating the statistical uncertainty.

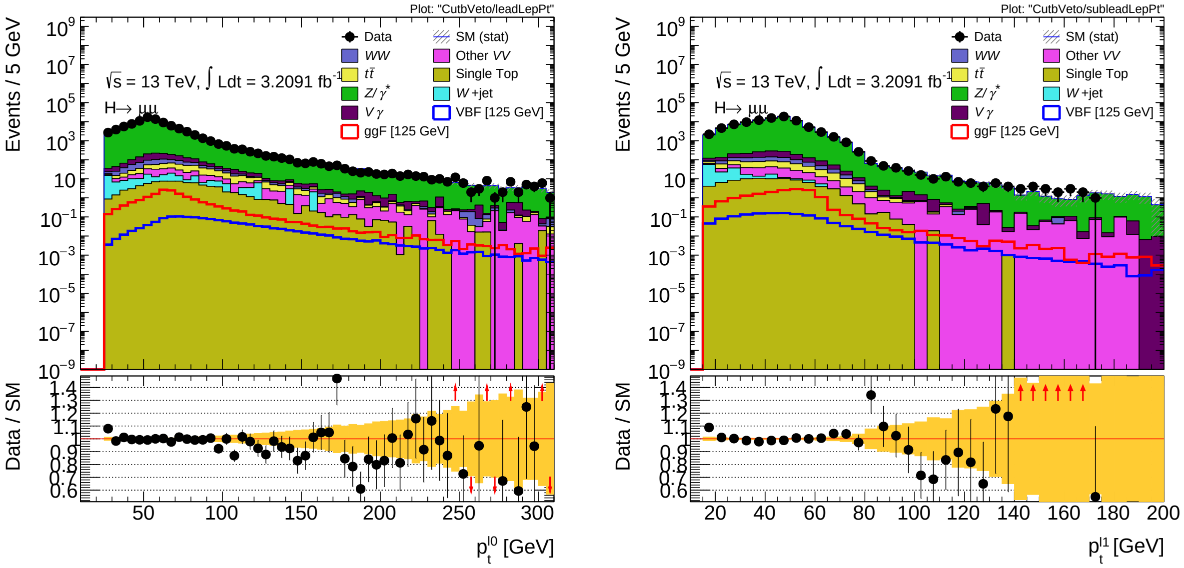

Figure 6.3: The transverse momentum of the leading (left) and subleading (right) muon. In the lower part of the plot the ratio between the data and the background MC is shown, with the yellow band indicating the statistical uncertainty.

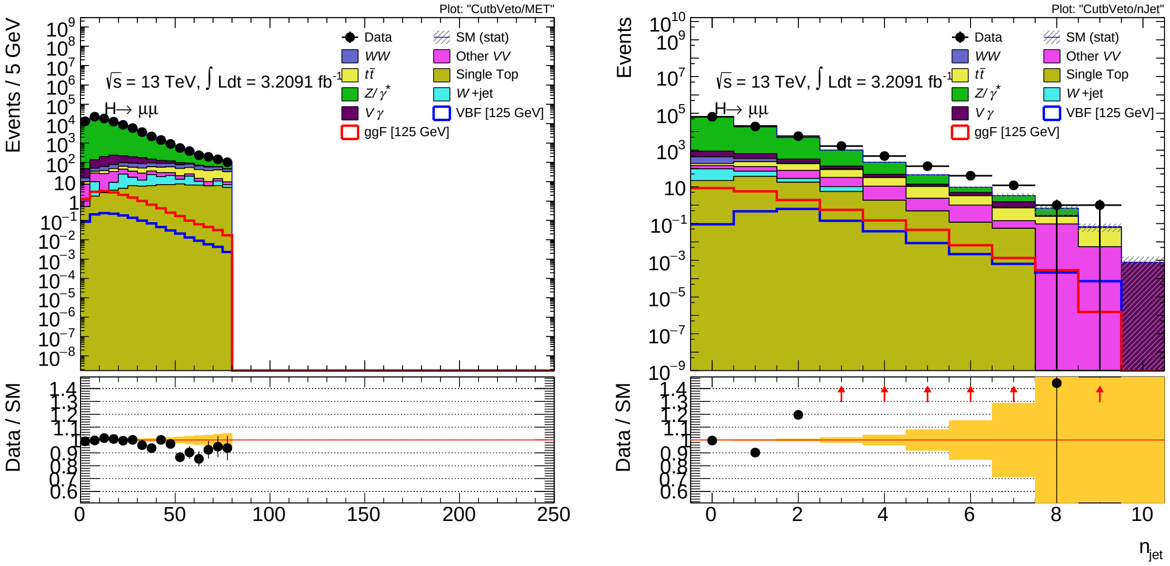

Figure 6.4: The missing transverse energy E_{T}^{miss} (left) and number of jets (right). In the lower part of the plot the ratio between the data and the background MC is shown, with the yellow band indicating the statistical uncertainty.

6.4.1 Signal regions

The six non-VBF signal regions are then defined as all combinations of the three $p_{\mathrm{T}}^{\mu\mu}$ rages and the central/non-central distinction. In all seven signal regions, the distribution of the invariant mass of the di-muon system $m_{\mu\mu}$ is used as the discriminating variable for the final statistical analysis. It is shown in figure 6.5 in the VBF region and the combined non-VBF regions, as well as those split up into the six $p_{\mathrm{T}}^{\mu\mu}/\eta_{\mu}$ regions in figure 6.6. The number of expected signal, background and data events, are shown in table 6.2.

$\sqrt{s} = 13TeV$, $\mathcal{L} = 3.2091fb^{-1}$, $\mu\mu$	VBF [125 GeV]	ggF [125 GeV]	Bkg.	Data
VBF	0.35 ± 0.00	0.16 ± 0.01	198.53 ± 8.87	168
Low $p_{\mathrm{T}}^{\mu\mu}$ central	0.01 ± 0.00	0.95 ± 0.02	9327.19 ± 60.84	9182
Low $p_{\mathrm{T}}^{\mu\mu}$ forward	0.03 ± 0.00	2.74 ± 0.03	37681.85 ± 125.87	37722
Mid $p_{\mathrm{T}}^{\mu\mu}$ central	0.07 ± 0.00	2.13 ± 0.03	6969.25 ± 52.36	6931
Mid $p_{\mathrm{T}}^{\mu\mu}$ forward	0.20 ± 0.00	5.93 ± 0.04	26806.50 ± 105.99	26727
High $p_{\mathrm{T}}^{\mu\mu}$ central	0.20 ± 0.00	1.41 ± 0.02	2534.23 ± 31.09	2502
High $p_{\mathrm{T}}^{\mu\mu}$ forward	0.51 ± 0.00	3.46 ± 0.03	8757.42 ± 59.64	8645

Table 6.2: Number expected VBF and ggF signal events, total background events and measured data events in the seven signal regions.

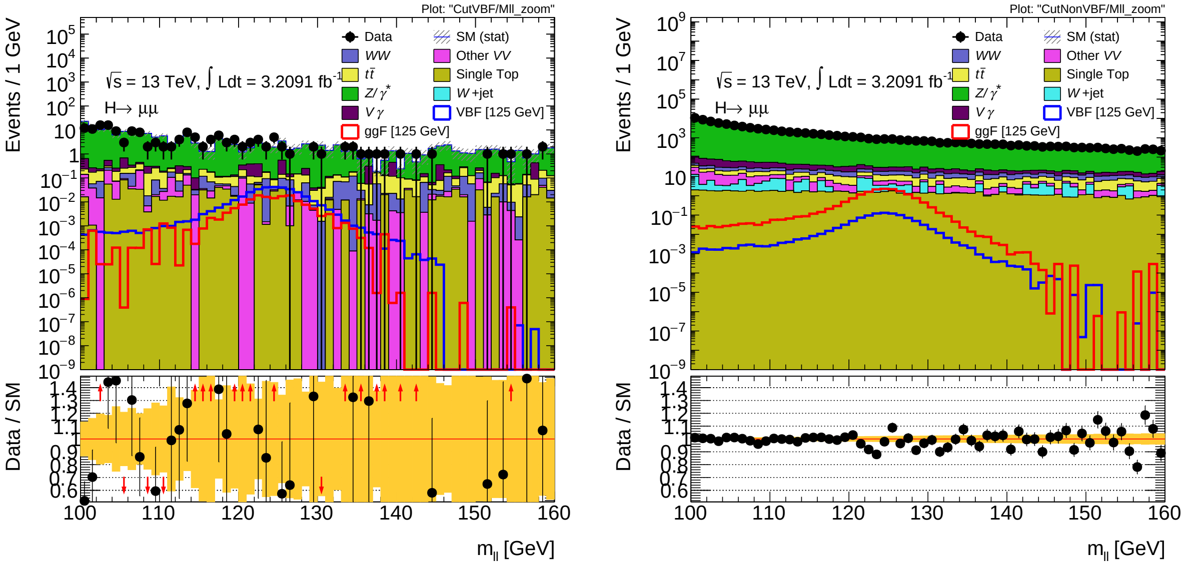

Figure 6.5: The invariant mass of the di-muon system $m_{\mu\mu}$ in the VBF signal region (left) and the combined non-VBF regions. The signal is shown for $m_{\mathrm{H}} = 125\,\mathrm{GeV}$. In the lower part of the plot the ratio between the data and the background MC is shown, with the yellow band indicating the statistical uncertainty.

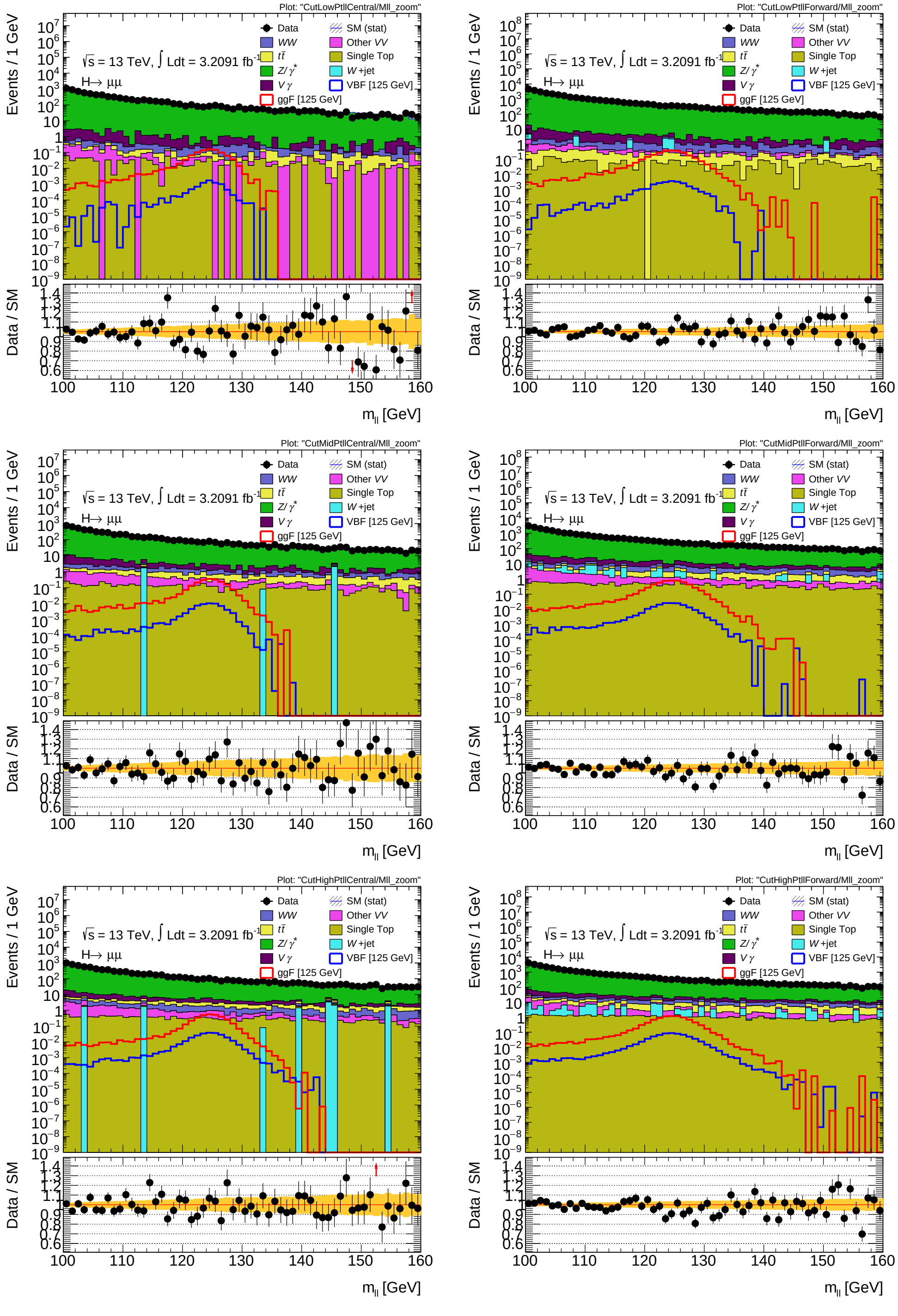

Figure 6.6: The invariant mass of the di-muon system $m_{\mu\mu}$ in the six non-VBF signal regions. The signal is shown for $m_{\mathrm{H}} = 125\,\mathrm{GeV}$. In the lower part of the plot the ratio between the data and the background MC is shown, with the yellow band indicating the statistical uncertainty.

Chapter 7

Background Processes

7.1 Drell-Yan Process

The Drell-Yan process is the annihilation of a quark with an antiquark and the subsequent creation of a lepton/antilepton pair, mediated by a Z-boson or a virtual photon, as depicted in figure 7.1. The initial state quarks may also radiate gluons leading to additional jets. Collectively, these processes are referred to as Z+jets.

There are the bulk of the irreducible background in this analysis with a high cross section and the same final state particles as the gluon fusion signal, i.e. two opposite charged muons. Their invariant mass spectrum $m_{\mu\mu}$ is falling with increasing mass, except for a broad peak around the mass of the Z boson $m_Z = 91.1876 \pm 0.0021$ GeV [17]. Its observed width is the combination of the natural Z boson width $\Gamma_Z = 2.4952 \pm 0.0023$ GeV [17] and the detector resolution. In the whole range of $100\,\text{GeV} < m_\text{H} < 160\,\text{GeV}$ which is considered in this analysis, Z+jets is the dominant background.

The Madgraph and Powheg samples were both used for comparison. In the plots shown, the Powheg generated Z+jets background is used.

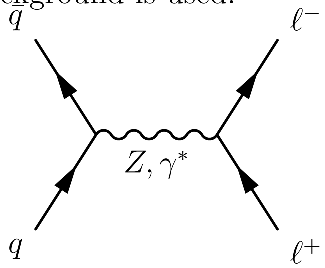

Figure 7.1: Feynman diagram of the $Z/\gamma^* \to \ell^+\ell^-$ process

7.2 Top Quark Production

Top quarks are at the LHC mostly produced in top/antitop pairs via the strong interaction, either by gluon gluon fusion or quark/antiquark annihilation. Figure 7.2 shows Feynman diagrams for these background processes, which together are called the $t\bar{t}$ background.

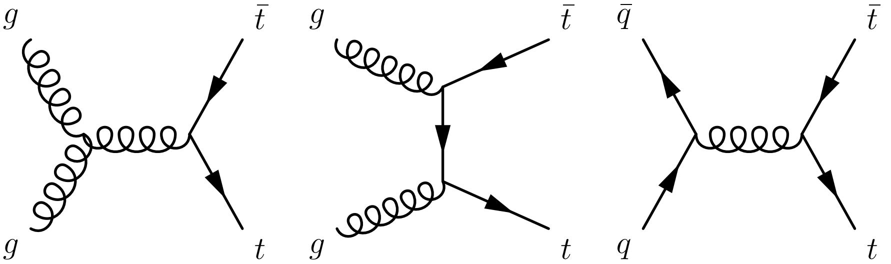

Figure 7.2: Feynman diagrams for top quark pair production at the LHC

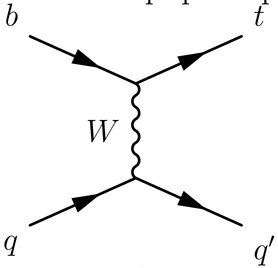

Figure 7.3: Example of Feynman diagram for single top quark production at the LHC

Single top quarks can also be produced via the weak interaction. Diagrams for the Single Top background are shown in figure 7.3.

A top quark will almost always decay into a b quark and a W boson, both of which may decay leptonically into states containing muons and thus become background for the H → $\mu\mu$ signal. However methods to tag and veto final states containing b quarks can be applied, as described in section 6.3.3

Since the top backgrounds typically contain high energy jets, they are especially relevant to the VBF signal, because they can look like the jets occuring in vector boson fusion.

7.3 Diboson Production

In events where two gauge bosons are created, referred to as diboson backgrounds, two opposite charged muons can occur. The largest contribution comes from W^+W^- pair production. Other diboson processes which are considered are production of WZ, $W\gamma$, $W\gamma^*$, ZZ and $Z\gamma$.

7.4 W+jets background

Processes which contain a leptonically decaying W boson and at least one jet are referred to as $W + jets$. In case one of those jets is misidentified as a muon, events from these processes are selected. Although this has a low probability, W+jets processes have such a high cross-section that a significant number of events remain. Because of this, single MC events are given high weights in the histogram which leads to a high statistical uncertainty. In addition this misidentification is generally not well modeled in MC, leading to a high systematic uncertainty.

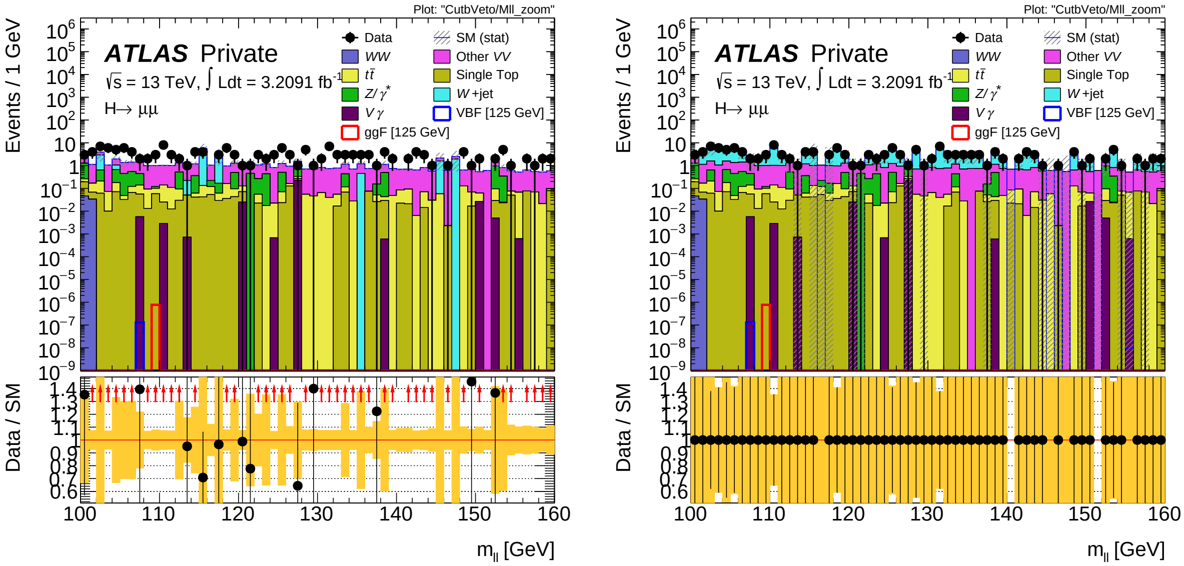

Figure 7.4: The invariant mass of the di-muon system $m_{\mu\mu}$ after all preselection cuts in the same sign region using MC W+jets (left) and the data driven method (right). In the lower part of the plot the ratio between the data and the background MC is shown, with the yellow band indicating the statistical uncertainty.In the left plot, the W+jets contribution in light blue only consists of single events leading to spikes in the distribution. In the right plot, the data-driven method gives a smother distribution for W+jets

Therefore a data-driven method is used to estimate this background using a data-driven method rather than MC. An event selection is applied that is identical to the nominal one, except that the charges of the two muons are required to have the same sign instead of the opposite one, as shown in the left plot of figure 7.4. It is assumed that the W+jets background is not affected by this change, since the muons are just misidentification.

As the data-driven W+jets background is then taken the difference between the measured data and all modeled MC non-W+jets backgrounds. In the same sign region, as seen in the right plot of the same figure, this looks by construction like there is perfect agreement between background prediction and data.

In all cuts and signal regions starting from the opposite sign cut the original MC

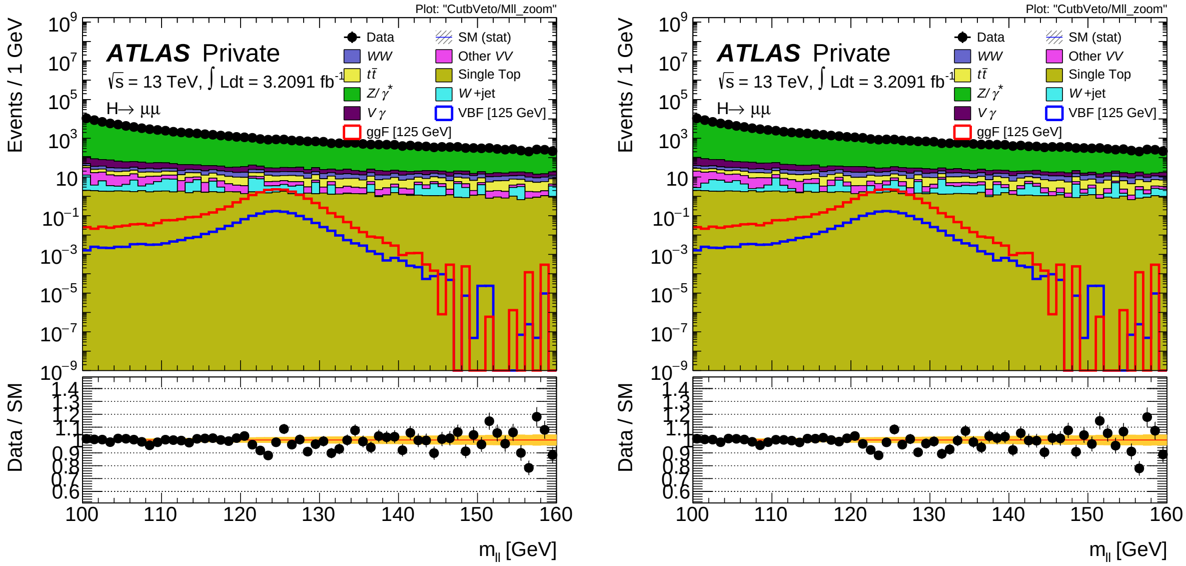

Figure 7.5: The invariant mass of the di-muon system $m_{\mu\mu}$ after all preselection cuts in the opposite sign region using the MC W+jets (left) and the data driven method (right). In the lower part of the plot the ratio between the data and the background MC is shown, with the yellow band indicating the statistical uncertainty.

W+jets background is then replaced by the corresponding same sign estimation. The $m_{\mu\mu}$ distribution is shown in figure 7.5 before and after this operation.

Chapter 8

Signal and Background Modeling

8.1 Signal Modeling

The H $\rightarrow \mu\mu$ signal is a fully reconstructible resonance, which manifests as a narrow peak in the dimuon invariant mass spectrum around the mass of the Higgs boson. The small natural width of the Higgs boson itself can be neglected. The detector resolution for the muon momentum measurement and reconstruction broadens this peak significantly. As shown in figure 8.1 this resolution $Z \rightarrow \mu\mu$ events it has been measured to be about 1.5% and 3% of the dimuon invariant mass $m_{\mu\mu}$ [62], and is therefore the dominating contribution of the overall signal width.

The shape of the signal peak is parametrized as the sum of a Gaussian distribution and Crystal Ball distribution as shown in equation 8.1.

$$f_{sig}(x, M, \sigma_{CB}, \alpha, n, \sigma_G) = f \cdot CB(x, M, \sigma_{CB}, \alpha, n) + (1 - f) \cdot exp\Big(- \frac{(x - M)^2}{2\sigma_G^2} \Big) \quad (8.1)$$

Here, x represents the running dimuon invariant mass. M represents the position of the peak, and is constrained to the same value in both the Gaussian and the Crystal Ball term. The fraction f of the contribution of the Crystal Ball term is fixed to 0.9 during the fit. Doing so increases the stability of the fit. For the same reason, in the Crystal Ball distribution the n parameter is fixed to 2.0, and the α parameter to 1.5. The parameters σ_G and σ_{CB} are the widths of the Gaussian and Crystal Ball distributions, respectively. Normalizing f_{sig} with the number of expected events N yields the full signal template.

All parameters that are not fixed are used as free parameters in a fit of f_{sig} to the $m_{\mu\mu}$ spectrum of the signal MC, consisting of the VBF and ggF processes, scaled to their theoretical prediction. This fit is performed separately in each signal region as defined in section 6.4.1, and for each available Higgs mass point.

For an assumed m_{H} of 125 GeV, the result of this fit is shown in figure 8.2. It can be observed that the signal peak is broader in the “Forward” regions than in the “Central” regions.

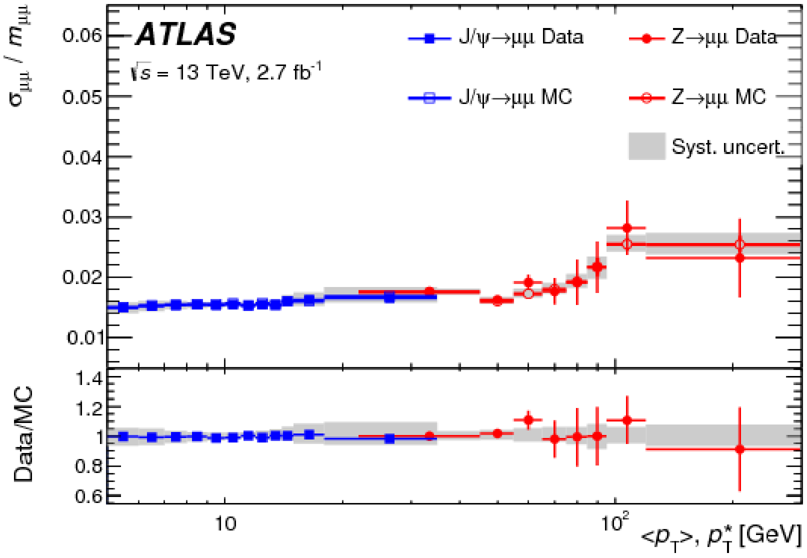

Figure 8.1: Relative invariant mass resolution for combined muons measured from $J/\Psi \to \mu\mu$ and $Z \to \mu\mu$ events taken from [62]. Data and MC lie so close that most markers overlap.

8.2 Signal Interpolation

Signal MC has only been generated for Higgs mass points from 100 GeV to 150 GeV, in steps of 5 GeV, due to limited computing resources. However, these steps are bigger than the width of the signal. In order not to be limited to the resulting eleven mass hypotheses, but to be able to perform a statistical test for masses in between, a special procedure is needed to generate an interpolated signal parametrization for arbitrary Higgs masses.

For each MC Higgs mass point m_{H}, the signal model described in section 8.1 is fitted to the Monte Carlo $m_{\mu\mu}$ spectrum in each signal region separately. This results in a set of parameters $\{N, M, \sigma_G, \sigma_{CB}\}_{m_{\mathrm{H}},region}$ for each fit. These are then interpolated using a second degree polynomial as a function of m_{H}. Figure 8.3 shows this fit for these four parameters in one signal region.

For an arbitrary m_{H}, the signal template is then obtained by using the interpolated parameters in the signal distribution $N(m_{\mathrm{H}}) \cdot f_{sig}(x, M(m_{\mathrm{H}}), \sigma_{CB}(m_{\mathrm{H}}), \alpha, n, \sigma_G(m_{\mathrm{H}}))$. Figure 8.4 shows these interpolated signal templates in comparison to the single mass point fits. They are a smooth continuation of the pattern in terms of shape and normalization.

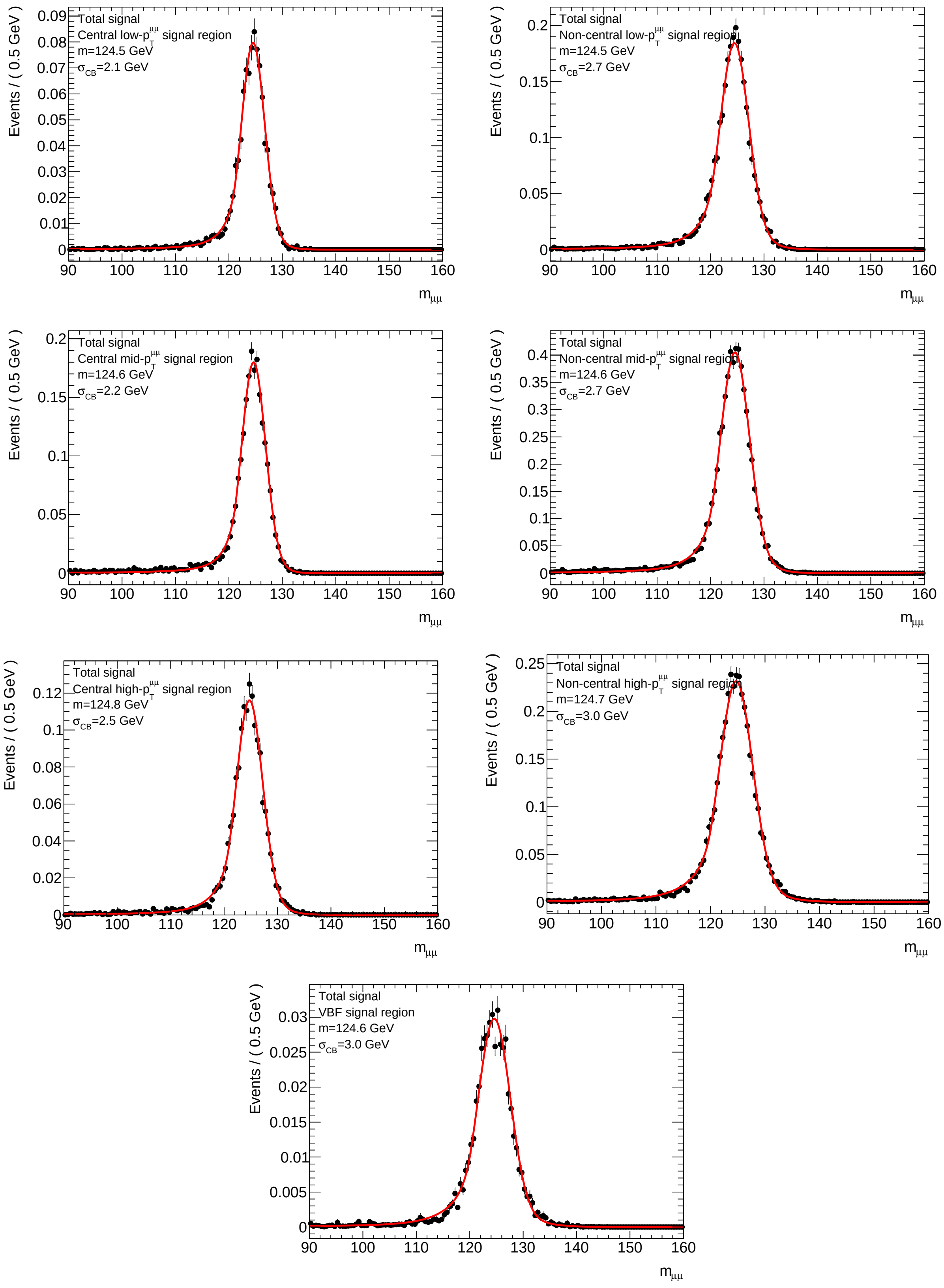

Figure 8.2: Fit of the signal model (solid red line) to the m_H =125 GeV signal MC (black dots) in all signal regions.

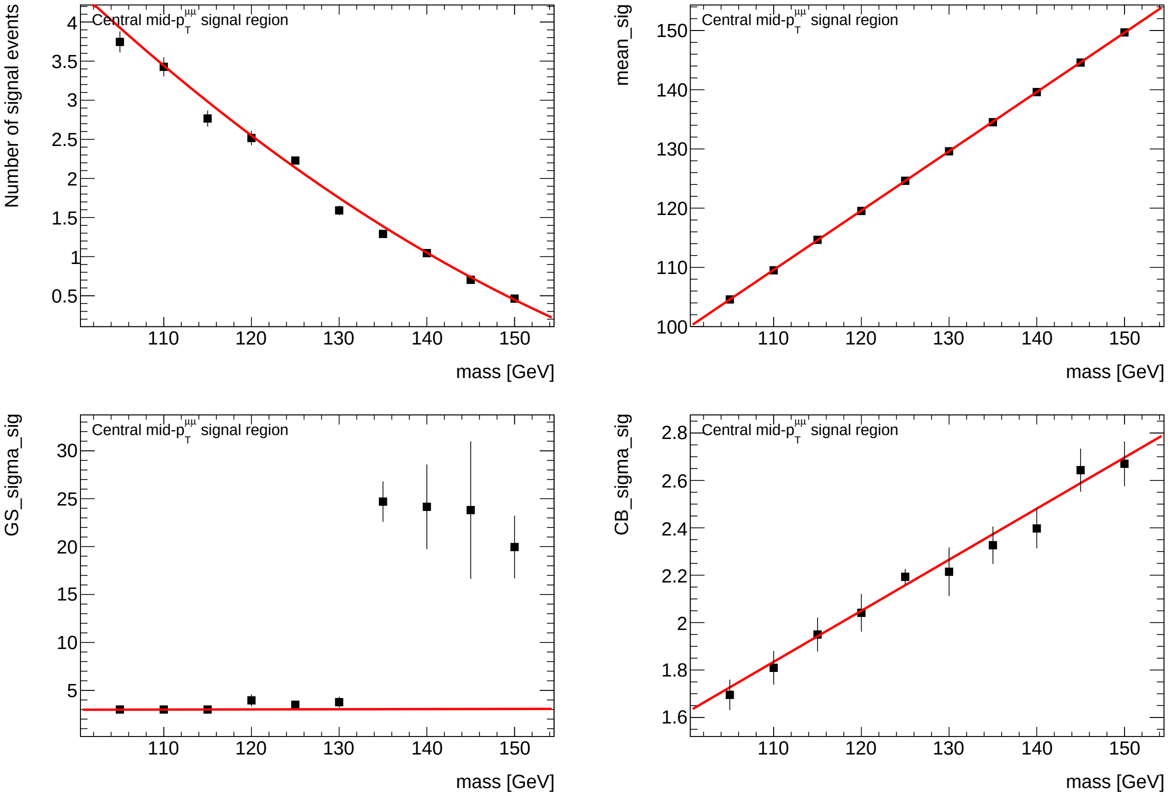

Figure 8.3: The parameters of the signal fit in the Central MidPtll region as a function of the MC Higgs mass (black): Number of signal events N (top left), position of the peak M (top right), width of the Gaussian (bottom left) and Crystal Ball (bottom right) distributions. The red graph shows the quadratic fit of each parameter,

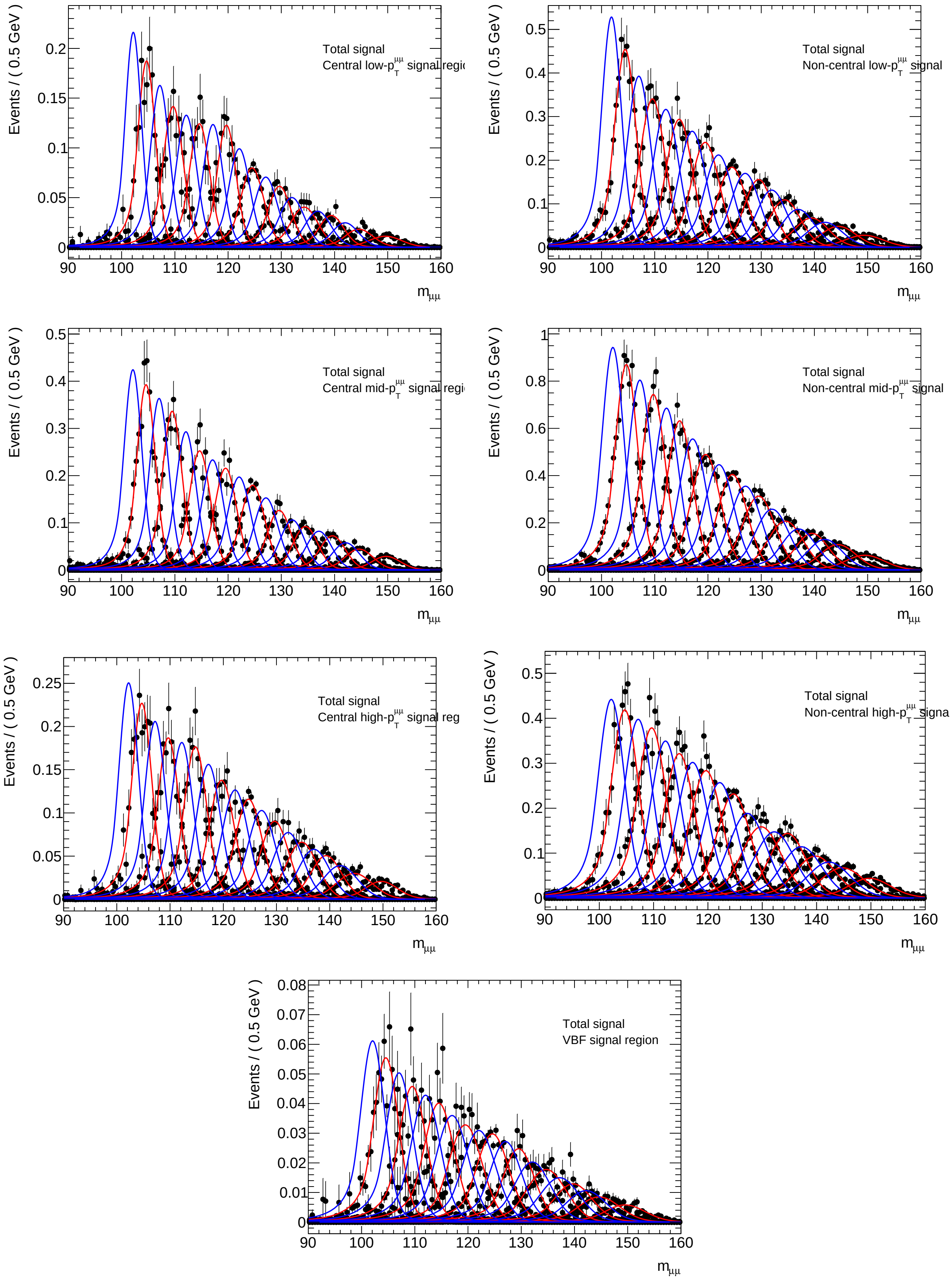

Figure 8.4: Comparison between the $m_{\mu\mu}$ distribution of the signal MC for all available mass points (black dots), the respective single mass point fits (red lines) and the interpolated signal templates (blue lines)

8.3 Background Modeling

Since the expected signal is so small, it is crucial that the background be modeled as correctly as possible. This section describes the method how to extract an estimation for the background from the measured data itself. That way systematic uncertainties in modeling and reconstruction of background MC are implicitly included.

To describe the background, a parametrized analytical function has been developed that can describe its shape. Scaled to the number of background events, this function is called the background model. It is dominated by the Z/Drell-Yan process, so a parametrization has been chosen that resembles in part the natural shape of the Z-peak. Since a number of cuts that distort the spectrum have been applied, it should not be expected to perfectly replicate it.

The model consist of a weighted sum of two probability density functions. Part of the first term is a non-relativistic Breit-Wigner shape, with f_{BW}^{norm} chosen to normalize its integral to 1.

$$BW(x, M_{BW}, \Gamma_{BW}) = f_{BW}^{norm} \cdot \frac{1}{(x - M_{BW})^2 + (\Gamma_{BW})^2} \tag{8.2}$$

The Breit-Wigner term is folded with a Gaussian function meant to represent detector resolution and reconstruction effects.

The second term is a falling exponential divided by a x^3 term, together normalized by the appropriately chosen constant f_{exp}^{norm} ,

The full background model is then chosen to be

$$f_B(x, M_{BW}, \Gamma_{BW}, \sigma_{GS}, f, B) = f \cdot (BW(M_{BW}, \Gamma_{BW}) * GS(\sigma_{GS}))(x) + (1 - f) \cdot f_{exp}^{norm} \frac{e^{B \cdot x}}{x^3} \tag{8.3}$$

In the Breit-Wigner term, the parameters for the mass M_{BW} and width Γ_{BW} are fixed at the known measured values of the Z-boson. The width of the Gaussian σ_{GS} is set in each signal region separately to the values given in table 8.1. Those values have been determined from fits to the background MC, and are then fixed to them to reduce the number of free parameters and to improve fit stability.

The fraction f of the first term, the parameter B in the exponential, and the overall normalization are left as free parameters of the fit. A χ^2 fit of the background model is then performed in all signal regions, and the fit quality evaluated.

There are several desired features in the background function. Firstly, it has to fit the background accurately and without bias. As seen in figure 8.5, the chosen background model consisting of the Breit-Wigner term and the exponential term with varying proportions does visibly fit the total background MC. A method to test the quality of a fit is to examine the pull distribution between fit and histogram. The pull g is defined, for each bin of the histogram, as the difference between fit and bin content, normalized by the uncertainty of the bin content. In case of good fit, the pulls are distributed in a standard normal distribution with standard deviation 1, centered around the origin [70].

	central	non-central
low-$p_{\mathrm{T}}^{\mu\mu}$	1.92	2.42
mid-$p_{\mathrm{T}}^{\mu\mu}$	1.94	2.45
high-$p_{\mathrm{T}}^{\mu\mu}$	2.21	2.72
VBF	2.72	

Table 8.1: Width of the Gaussian term σ_{GS} in $f_B(x, M_{BW}, \Gamma_{BW}, \sigma_{GS}, f, B)$ in units of GeV

A fit of a Gaussian distribution to the pull distributions of each signal region is shown in figure 8.6. In all of them, the fit parameters agree with this quality criterion within the uncertainty of the fit. The chosen background parametrization is therefore deemed as valid and unbiased.

8.4 Combined signal+background model

The combined model is simply the addition of the background model and the signal model, the later scaled with the additional free parameter μ. The parameter μ describes the strength of the signal relative to the SM expectation.

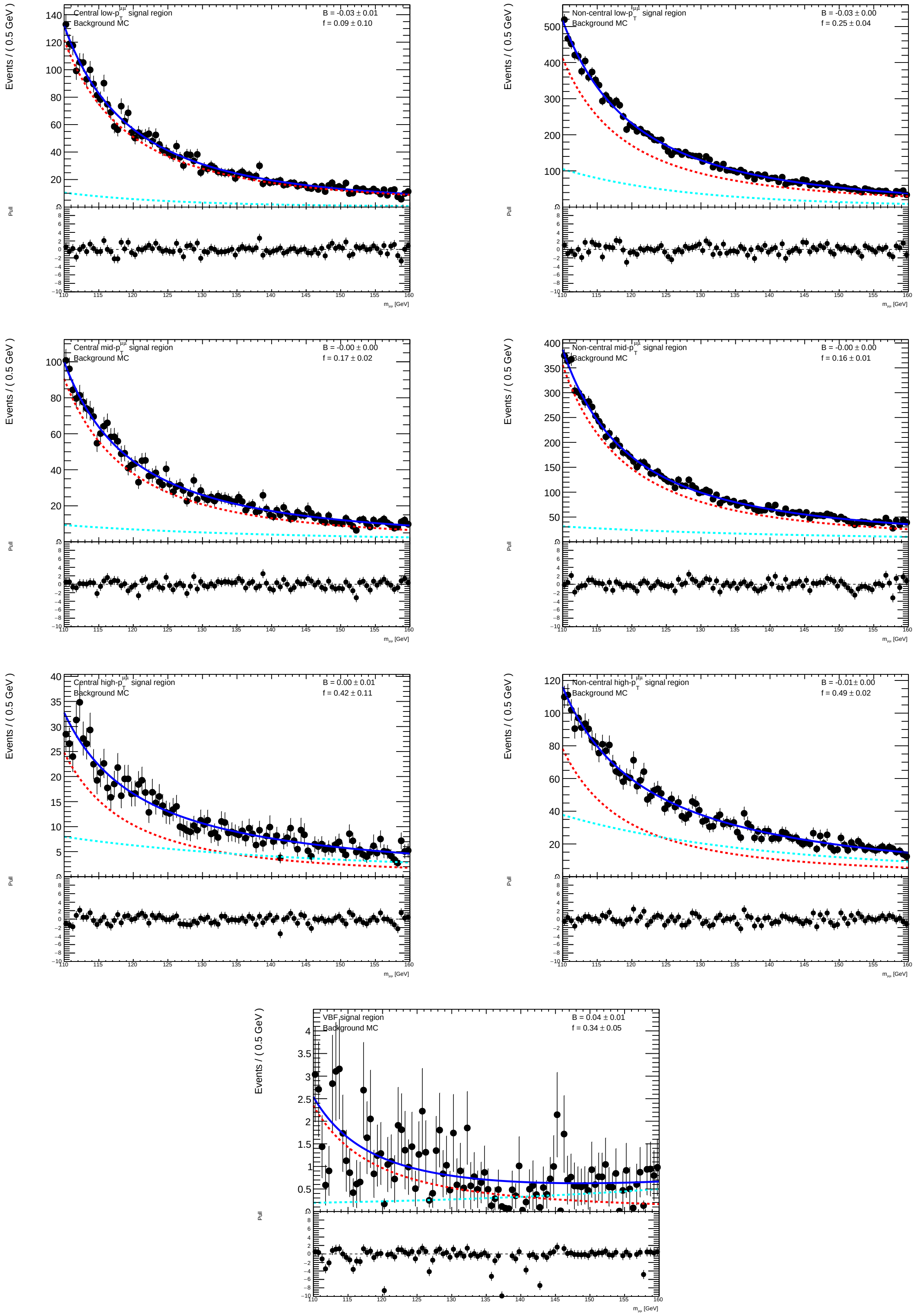

Figure 8.5: Fit of the full background model (solid blue line) to background MC (black dots) in the upper part of each plot, pull between model and MC in the lower part of each plot, shown for all seven signal regions. Shown separately are the Breit-Wigner term (dashed red line) and the exponential term (dashed turquoise line).

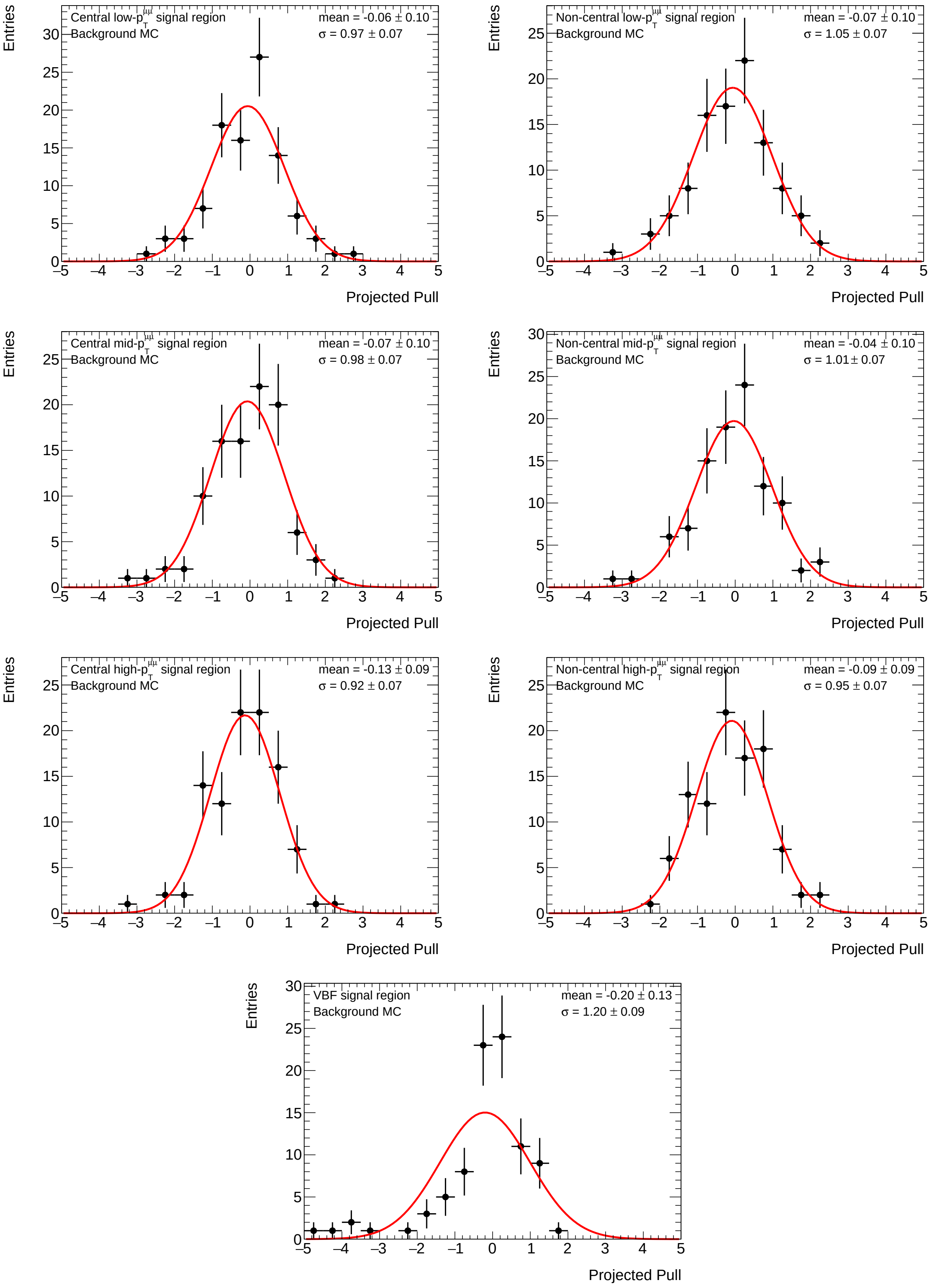

Figure 8.6: Distribution of the pulls between background fit and background MC (black) and fit of normal distribution to pull distribution (red line), shown for all seven signal regions

Chapter 9

Systematic Uncertainties

This chapter describes the sources of uncertainty in the modeling of the H $\rightarrow \mu\mu$ signal. This includes both uncertainties in the theoretical modeling of the two signal processes and uncertainties arising from uncertainties of the experimental conditions and performance of the ATLAS detector. Since the background estimation is extracted from the fit to the measured data, its uncertainty is implicitly included.

9.1 Theoretical Uncertainties

Theoretical uncertainties on the production cross sections for the ggF and VBF signal and the branching ratio of H $\rightarrow \mu\mu$ are provided from the LHC cross section working group [71][41]. They arise from uncertainties on higher-order corrections to the cross sections which are estimated by varying QCD renormalization and factorization scales, They also include uncertainties on the parton distribution functions and strong coupling constant α_s. These are calculated by changing the CT10, the PDF set used, to its systematic variations provided in the PDF set. The uncertainties related to the modeling of multi-parton interactions in the MC event generation are estimated by switching it off during the event generation.

For the ggF signal, uncertainties on the distribution of the Higgs p_{T} have been evaluated by varying the QCD renormalization, factorization and resummation uses in the Hres program. The dimuon transverse momentum $p_{\mathrm{T}}^{\mu\mu}$, which for the signal is the Higgs p_{T}, is used to split the signal up into the $p_{\mathrm{T}}^{\mu\mu}$-categories as described in section 6.4.1. A change in this distribution therefore leads to migration between the signal regions, resulting in correlated changes in signal yields therein, but no change in the total signal yield for all regions. Table 9.1 gives an overview over these uncertainties for the $m_{\mathrm{H}} = 125\,\mathrm{GeV}$ signal.

9.2 Experimental Uncertainties

In addition to the theoretical uncertainties, systematic uncertainties arise from imperfect knowledge of the experimental conditions. This includes the properties of the proton beams

	ggF	VBF
Branching ratio	±1.23%	±1.23%
QCD scales	4%	0.8%
PDF and α_s	1.9%	2.1%
Multi-parton interactions	9%	4%
Higgs p_T	$> 22\%$	-

Table 9.1: Sources of theoretical uncertainties on the signal yield for an assumed $m_\mathrm{H} = 125\,\mathrm{GeV}$. The migration from uncertainties arising from Higgs p_T uncertainties are separated by signal region, given is only the maximum value.

as well as the performance of the ATLAS detector hardware and reconstruction software. In order to estimate their extent, each considered source of uncertainty has associated to it one or more associated parameters. These can be varied and affect the resulting obtained kinematic distributions.

9.2.1 Luminosity and Pileup

The uncertainty in the integrated luminosity is ±2.1%. It is derived, following a methodology similar to that detailed in [24] from a calibration of the luminosity scale using x-y beam-separation scans performed in August 2015.

The systematic effects of the rescaling in the pileup re-weighting process described in section 6.2 is estimated by varying the scale factor from $^1/_{1.16}$ to $^1/_{1.09}$ and $^1/_{1.23}$.

9.2.2 Muons

The dominant experimental uncertainties are the uncertainties concerning muons. Systematic variations for the efficiency of the muon trigger, the efficiency of reconstruction muons, and the efficiency of the muon isolation are evaluated, each of them one parameter for statistical and systematic components.

Three variations are used for correction of the momentum scale and the resolution of muon reconstruction, both in the inner detector and the muon spectrometer.

9.2.3 Jets and Missing Transverse Energy

For the selected jets, one systematic variation is used for the jet energy resolution [72] and a set of three parameters for the jet energy scale. There are three systematic parameters associated to the calibration of the *b*-jet tagging, one each related uncertainties of *b*-jet, *c*-jet, light quark flavor tagging. Two additional parameters are used to quantify the uncertainties in the calculated of missing transverse energy [73].

9.2.4 Combination and Interpolation

The impact of these systematic variations the distribution of $m_{\mu\mu}$ is evaluated for each Higgs mass point in all seven signal regions separately. For each of them, a combined uncertainty is calculated in the following way. For each variation of a systematic parameter, the deviation of the $m_{\mu\mu}$ distribution with respect to the nominal distribution is calculated. All upward deviations and downward deviations are then added separately in quadrature into an envelope around the nominal distribution. The separation into upward and downward is performed to account for possible asymmetries of the deviations. From the envelope, a total relative up and down uncertainty on the signal yield is calculated, as listed in table 9.2 for $m_{\mathrm{H}} = 125\,\mathrm{GeV}$. As expected the uncertainty is highest in the VBF region because of additional jet related systematics when requiring jets and cuts on their kinematics.

In order to illustrate the different sources of uncertainty, related systematic variations are summed up by this method in groups and their the impact shown in figure 9.1.

Signal region	yield	up [%]	down [%]
Low $p_{\mathrm{T}}^{\mu\mu}$,Forward	2.73	+1.42	-1.73
Low $p_{\mathrm{T}}^{\mu\mu}$, Central	0.95	+2.10	-2.40
Mid $p_{\mathrm{T}}^{\mu\mu}$, Forward	6.04	+1.70	-1.92
Mid $p_{\mathrm{T}}^{\mu\mu}$, Central	2.16	+2.20	-2.51
High $p_{\mathrm{T}}^{\mu\mu}$, Forward	3.93	+2.15	-2.14
High $p_{\mathrm{T}}^{\mu\mu}$, Central	1.59	+2.57	-2.65
VBF	0.50	+10.8	-0.17

Table 9.2: Total signal yield for an assumed $m_{\mathrm{H}} = 125\,\mathrm{GeV}$ and systematic uncertainties in percent thereon, summed separately in quadrature for upward and downward deviation. Shown for all signal regions as defined in section 6.4.1

Analogous to the interpolation of the signal shape and normalization as described in section 8.2, the total combined systematic signal uncertainties in each signal region are interpolated linearly as a function of m_{H}. The resulting uncertainty on the signal for an arbitrary Higgs mass is included in the statistical treatment in section 10.

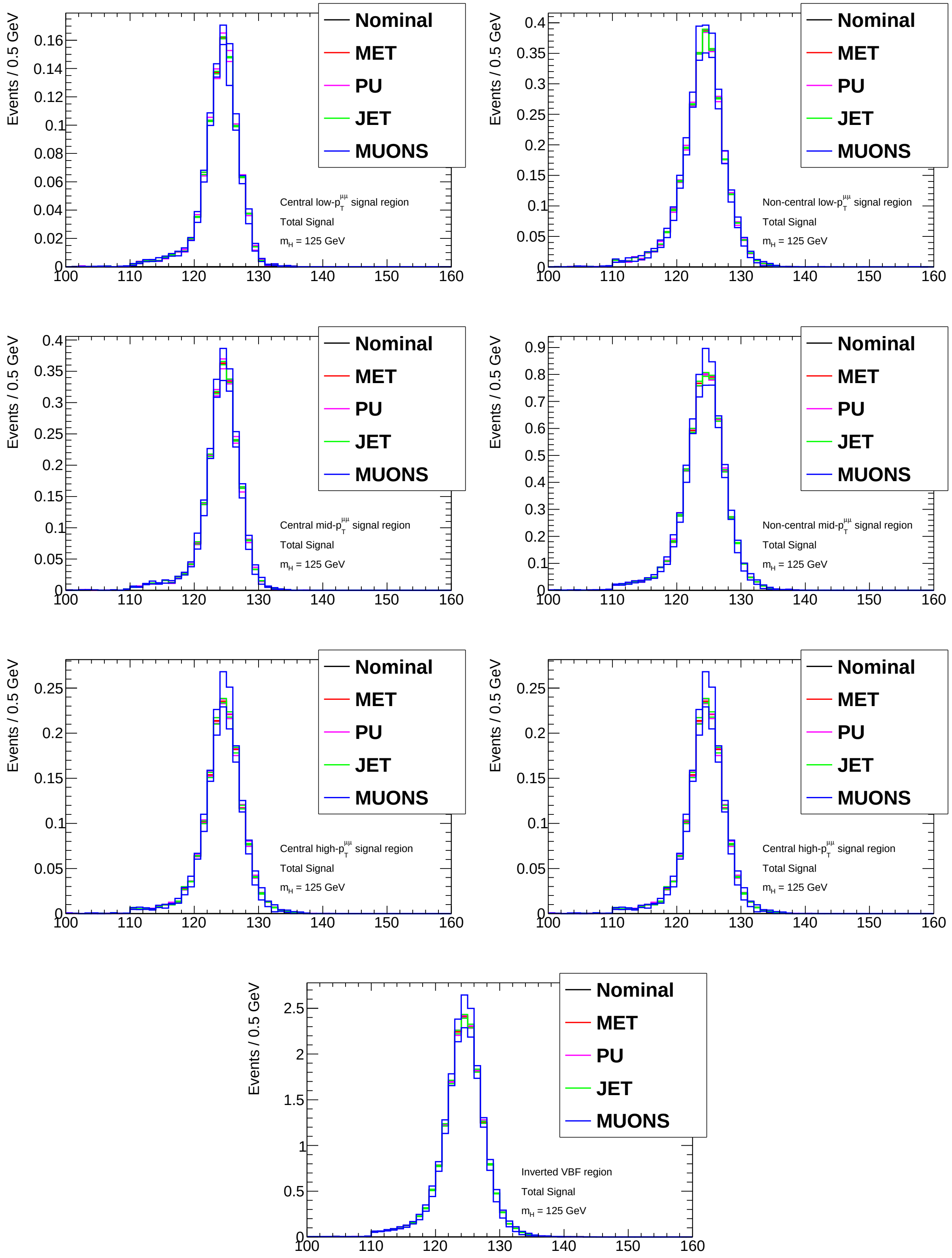

Figure 9.1: Invariant di-muon distribution of the total nominal (black) $H \to \mu\mu$ signal and with its systematic variations applied (colored), shown for $m_{\mathrm{H}} = 125\,\mathrm{GeV}$ in all seven signal regions. PU stands for Pileup re-weighting.

Chapter 10

Statistical Methods

This section discusses the statistical methods and definitions used to derive the results presented in section 11. The framework of hypothesis testing is introduced and applied to the search for H → $\mu\mu$ decays, including the determination of an exclusion limit on the signal strength.

10.1 Hypothesis Testing

The search for the H → $\mu\mu$ signal is formulated mathematically in the framework of hypothesis testing, a central aspect of statistical theory. In this case, one hypothesis is that there are no H → $\mu\mu$ decays, only the known SM backgrounds b. This is called the null-hypothesis. An alternative hypothesis postulates the existence of the signal in addition to the background. It can be generalized into a class of hypotheses that scale the signal by a real number μ, the signal strength parameter. The parameter μ is defined as the ratio of measured number of signal events to the number of signal events expected in the Standard Model.

All hypotheses can then be expressed as $\mu \cdot s + b$. The background only hypothesis corresponds to $\mu = 0$, the SM expectation to $\mu = 1$, and all other values of μ to other possible signal strengths. To quantify the level of agreement or disagreement between a hypothesis and the measured data, the test statistic $\tilde{q}_\mu$ is introduced. It is a function of the measured data, the distributions of expected signal and background events and all model parameters, in such a way that higher values of $\tilde{q}_\mu$ mean more incompatibility between the measurement and the tested hypothesis.

The so called p-value for a given hypothesis is then defined as the probability under this hypothesis that the test statistic is as high or higher than the one calculated from the observed data, denoted as $\tilde{q}_{\mu,obs}$. One therefore integrates the probability distribution $\tilde{q}_\mu$ under the given hypothesis, $f(\tilde{q}_\mu|\mu)$, over all values of $\tilde{q}_\mu > \tilde{q}_{\mu,obs}$, to obtain the p-value:

$$p_\mu = \int_{\tilde{q}_{\mu,obs}}^{\infty} f(\tilde{q}_\mu|\mu) d\tilde{q}_\mu \tag{10.1}$$

If the p-value for a given hypotheses becomes too small, the hypotheses is rejected for being incompatible with the observed data.

When $f(\tilde{q}_\mu|\mu)$ is not known in closed form, which is mostly the case in particle physics, it has traditionally been probed by generating Monte Carlo pseudo-experiments, also called toy Monte Carlo. From an initial MC template a great number of histograms is generated with their corresponding bins filled according to Poission distributions around the template bin contents.

Their corresponding test statistic is then calculated. The distribution of the test statistic in the toy MC is then taken as an approximation of its true distribution. This is however computationally expensive, and can become unfeasible for more complicated models. For some choices of the test statistic there exist asymptotic formulae [74] which approximate its probability distribution using only one representative histogram called the Asmiov[1] dataset. This ansatz is used in this analysis.

The test statistic used in this analysis is the following form of log-likelihood ratio:

$$\tilde{q}_\mu = \begin{cases} -2\ln\frac{L(\mu,\hat{\hat{\theta}}(\mu))}{L(\hat{\mu},\hat{\theta})} & 0 \leq \hat{\mu} \leq \mu \\ 0 & \hat{\mu} > \mu \\ -2\ln\frac{L(0,\hat{\hat{\theta}}(0))}{L(\hat{\mu},\theta\hat{(\mu)})} & \hat{\mu} < 0 \end{cases} \tag{10.2}$$

The likelihood function L depends on the result of the combined fit of signal+background model as described in section 8.4. Its explicit form is described later in section 10.3.

In the definition of the test statistic, θ is the set of the so called nuisance parameters. Those are free parameters that are used in the fit, but are not of interest themselves. Specifically the systematic uncertainties are treated as nuisance parameters. The set values $\hat{\theta}$ and $\hat{\mu}$ are the best fit values of these parameters when both are allowed to float free. $\hat{\hat{\theta}}$ is the best fit for a floating θ but for a μ fixed to a specific value.

In particle physics it is common to report deviations from the null-hypothesis not in terms of the corresponding p-value, p_0, but as an equivalent significance level Z. It is defined in terms of the normal Gaussian distribution. A normal random variable has, when found at Z standard deviations above its mean, an upper-tail probability equal to p. It is therefore calculated from the inverse of the cumulative distribution of the standard Gaussian distribution Φ as

$$Z = \Phi^{-1}(1-p). \tag{10.3}$$

In particle physics it has become customary to require a significance of at least $Z > 3$ before claiming to see evidence of a new phenomenon, and at least $Z > 5$ to claim its discovery, as was the case with the discovery of the Higgs boson.

---

[1] This name derives from the short story Franchise by Isaac Asimov, in which the result of an election is extrapolated from an interview with a single voter.

10.2 Exclusion Limit

This analysis uses the modified frequentist method, or CL_s method [75] to quantify how much each hypothesis is favored or disfavored. The confidence level in a given μ-hypothesis is defined as the probability that the test-statistic is less or equal than the observed value $\tilde{q}_{\mu,obs}$. For the signal+background hypothesis ($\mu = 1$) the confidence level is

$$CL_{s+b} = \int_{-\infty}^{\tilde{q}_{\mu,obs}} f(\tilde{q}_{s+b}|s+b) d\tilde{q}_{s+b} \tag{10.4}$$

Small values of CL_{s+b} indicate poor compatibility between the observed data and the signal+background hypothesis. In an analogous way the confidence level in the background-only hypothesis is given as

$$CL_b = \int_{-\infty}^{\tilde{q}_{\mu,obs}} f(\tilde{q}_b|s+b) d\tilde{q}_b \tag{10.5}$$

The modified frequentist confidence level CL_s is then defined as the ratio of the two:

$$CL_s = \frac{CL_{s+b}}{CL_b} \tag{10.6}$$

The signal hypothesis will then be considered excluded at the confidence level CL when

$$1 - CL_s \leq CL. \tag{10.7}$$

The CL used typically, as it is in this analysis, is 95%. Generalizing from the background-only ($\mu = 0$) and signal+background ($\mu = 1$) hypotheses, a confidence limit can be calculated for any signal strength hypothesis. Since stronger signals can be more easily excluded, there will be one highest μ, for which the corresponding hypothesis can be excluded at this confidence level. This value of μ is defined as the upper exclusion limit on the signal strength.

10.3 Likelihood Function

As mentioned in section 6.4, the data is split up into seven signal categories. A simultaneous fit is performed in all categories to extract the results. So the complete likelihood is the product of the individual likelihood in each category

$$L\left(\mu, \theta = \bigcup_{c=1}^{n_{cat}=7}\right) = \prod_{c=1}^{n_{cat}=7} L_c(\mu, \theta_c) \tag{10.8}$$

where n_{cat} is the number of signal categories (in this analysis $n_{cat} = 7$), and θ_c the set of nuisance parameters in category c.

Each category likelihood is the likelihood of a binned histogram, so the product of the likelihood in each bin is given as

$$L_c(\mu, \theta_c) = \prod_{k=1}^{N_c} \mathcal{L}_c(m_{\mu\mu}(k), \mu, \theta_c), \tag{10.9}$$

where k runs over the bin numbers, $m_{\mu\mu}(k)$ is the value of $m_{\mu\mu}$ (k), and $\mathcal{L}_c$ is the single-bin likelihood. It is computed from the observed data distribution and the combined signal+background model and includes the systematic signal uncertainties discussed in section 9 in the form of nuisance parameters.

Chapter 11

Results

The procedure described in section 10 is executed for each Higgs mass hypothesis between 115 GeV and 145 GeV in steps of 1 GeV. For each mass point, the signal distribution is constructed from the template developed in section 8.1 and combined with the background model from section 8.3. The resulting signal+background model is then fitted to the data $m_{\mu\mu}$ spectrum and the statistical treatment applied.

Figure 11.1 shows the resulting values of p_0 as a function of m_H. The high values of p_0 indicate a good agreement between the background-only model and the data, indicating no significant excess of signal-like events. This is compatible with the expected sensitivity of this analysis, which did not predict significant excesses for a Standard Model-like Higgs boson with the amount of data used.

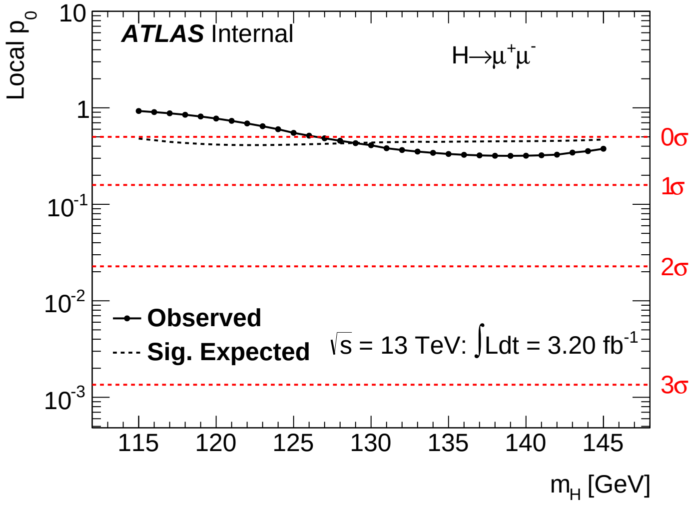

Figure 11.1: Expected (gray dashed line) and observed (black dots) p_0 value as a function of m_H. The dashed red lines indicate the corresponding significance Z.

In addition the upper limit on the signal strength parameter μ at a confidence level of 95% is calculated as a function of m_H as shown in figure 11.2. The observed limit mostly agrees within one standard deviation σ with the limit expected for a SM Higgs boson, and never disagrees more than two σ. For a Higgs mass $m_{\mathrm{H}} = 125\,\mathrm{GeV}$ a signal strength greater than 8.7 can be excluded by this measurement, compared to an expected exclusion of 9.1. Table B.1 lists the exclusion limits for the whole range in 1 GeV steps.

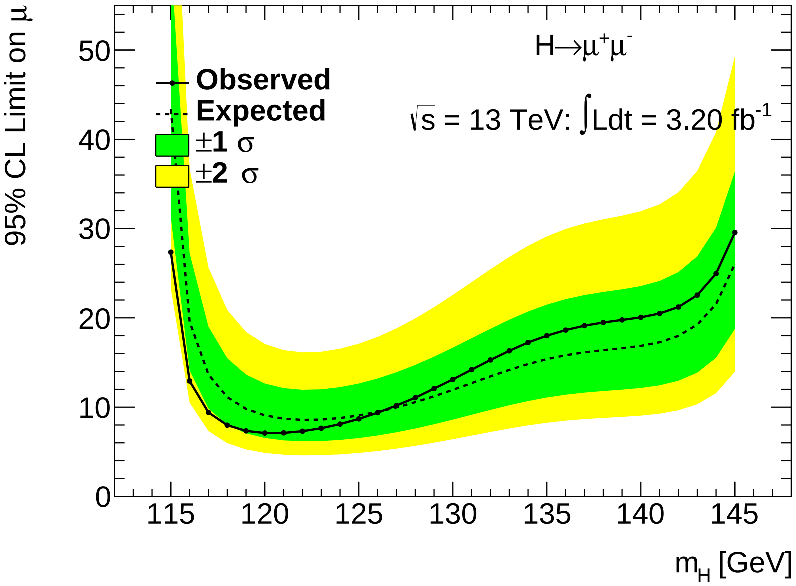

Figure 11.2: Expected (dashed line) and observed (solid line and dots) 95% CL limit on $\mathrm{H} \rightarrow \mu\mu$ signal strength. The dashed black line represents the expected values, with the green (yellow) bands showing the 1 (2) σ uncertainties on the expected values.

As seen in table 6.2 the contribution of the VBF signal to the total signal yield is relatively small. So with little loss of exclusion power the result can be converted into a search for a more generic scalar boson decaying into a pair of muons. To do this, the VBF contribution is set to zero, and an exclusion limit derived not in terms of signal strength μ but in terms of cross section multiplied by branching ratio. The resulting limit as a function of boson mass is shown in figure 11.3.

Figure 11.4 shows a contour plot of exclusion limits for another modified signal hypothesis. In this model the contribution of VBF signal was artificially scaled by a factor between 0 and 30, called here the VBF signal multiplier, while the ggF contribution was left to its SM prediction. A region of very high additional VBF contribution can be excluded. For a Higgs mass $m_{\mathrm{H}} = 125\,\mathrm{GeV}$ this exclusion extends from values greater than 24 times the SM VBF prediction.

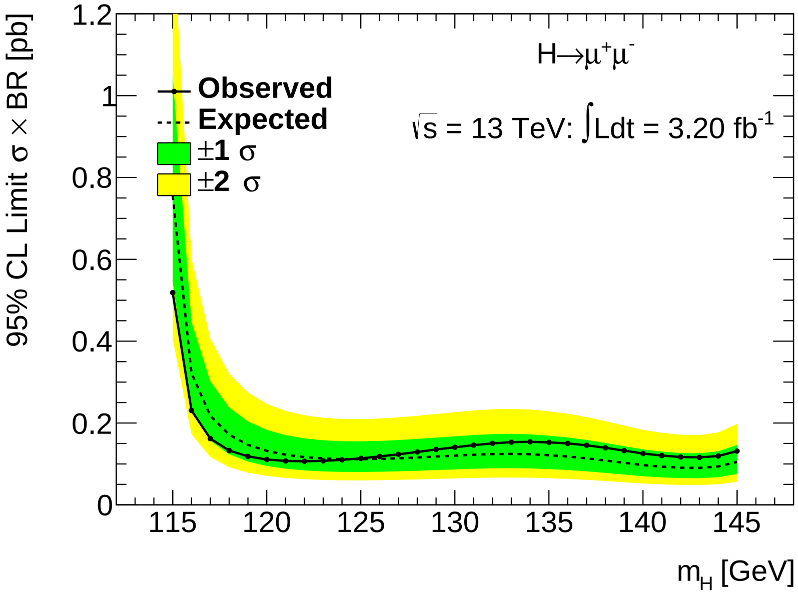

Figure 11.3: Expected (dashed line) and observed (solid line and dots) 95% CL limit on $\sigma \times BR$ for a more generic scalar Boson decaying into a dimuon final state. The dashed black line represents the expected values, with the green (yellow) bands showing the 1 (2) σ uncertainties on the expected values.

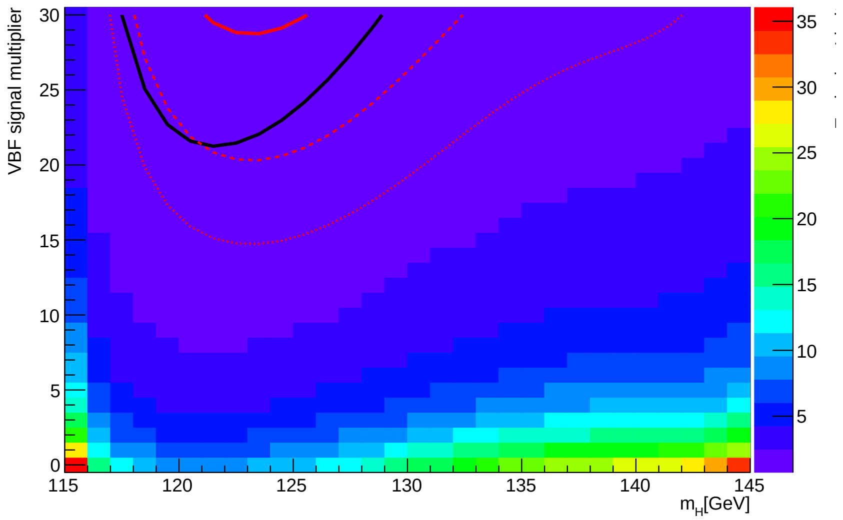

Figure 11.4: Contour plot of 95% CL exclusion limits on VBF enriched models as a function of $m_{\rm H}$ and the VBF signal multiplier. The black line shows the observed limit, the red line the expected limit, and the dashed and dotted red lines the 1σ and 2σ uncertainties on the expectation. The color value represents the 95% exclusion on the total signal strength μ for each model.

Chapter 12

Summary and Outlook

After the discovery of the top quark in 1995 [76] and the tau neutrino in 2000 [77], the Higgs boson was the last elementary particle predicted by the Standard Model that had not been found yet. Since its discovery in 2012 we now have evidence for its associated Higgs field and the BEH mechanism, solves the problem of giving mass to the gauge bosons of electroweak theory. All studies of the Higgs boson so far have found its characteristics to be consistent with the predictions of the SM.

Among those Higgs properties are the decay rates into its various decay products, which have been started to get measured in recent years. In figure 12.1 the measured signal strengths are shown for a number of Higgs decay channels. They are compatible with a Standard Model Higgs boson (signal strength $\mu = 1$).

Figure 12.2 shows these in terms of the reduced coupling strengths for both fermions and vector bosons. All measurements so far agree very well with the SM predictions over multiple orders of magnitude in particle mass.

This thesis presents the search for Higgs boson decays into muon-antimuon pairs using data collected in 2015 by the ATLAS experiment during proton-proton collisions at a center of mass energy of 13 TeV. The analyzed data corresponds to a total integrated luminosity of $3.2\,\mathrm{fb}^{-1}$.

The direct $\mathrm{H} \rightarrow \mu\mu$ decay leads to two opposite charged muons with high transverse momentum in the final state. If the Higgs boson was produced via Vector boson fusion, there are also two energetic hadronic jets that are missing in gluon-gluon fusion. In both cases the whole kinematics of the event can be reconstructed. This signal manifests itself in the dimuon invariant mass spectrum as a peak around mass of the Higgs boson.

A fit-based method is developed to search for this peak atop a large background, dominated by the Z+jets process. After the selection of signal-like events the dimuon invariant mass spectrum is used as the discriminating variable. From fits to signal MC, a parametrization of the signal distribution is developed in form of a closed form expression for the shape and amplitude of the signal as a function of Higgs mass. Together with a parametrized model of the background, a combined fit is performed in seven signal regions. No significant excess has been found.

Exclusion limits on the strength of the SM $\mathrm{H} \rightarrow \mu\mu$ decay are calculated. For a SM

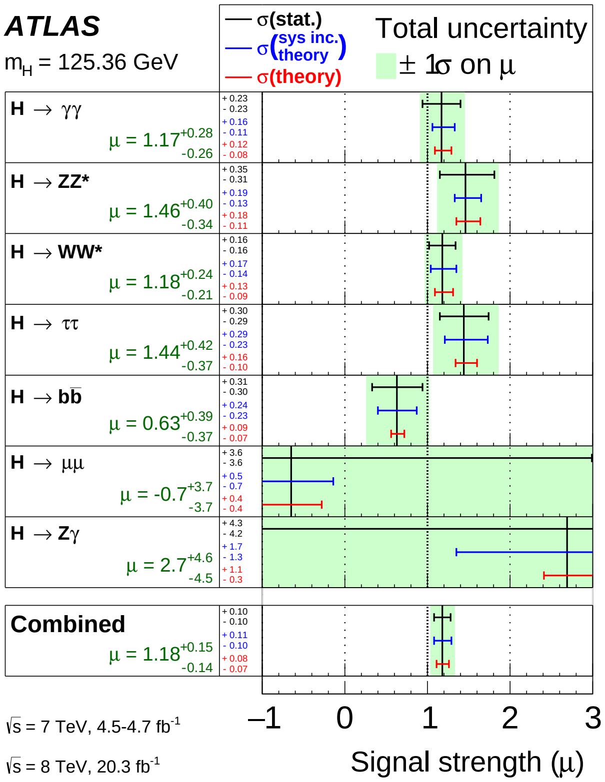

Figure 12.1: The observed signal strength for Higgs boson decays at ATLAS. The black vertical lines show the best-fit values. The green bands represent the total uncertainty, with the black, blue and red vertical lines showing the statistical, total systematic and systematic theory uncertainties, respectively. [78]

Higgs boson with a mass of $m_{\mathrm{H}} = 125\,\mathrm{GeV}$, a signal strength of more than 8.7 can be excluded at the 95% confidence level, with an expected limit of 9.1.

An updated analysis using data corresponding to $13.2\,\mathrm{fb}^{-1}$ integrated luminosity [79] yields exclusion limits of 4.4 (observed) and 5.5 (expected) times the Standard Model expectation.

The LHC and ATLAS are scheduled to keep taking data, and upgrades are planned that promise to yield hundreds of inverse femtobarn of integrated luminosity. At the moment the searches for $\mathrm{H} \to \mu\mu$ decays are currently severely statistically limited. The future data is expected to lift this limitation.

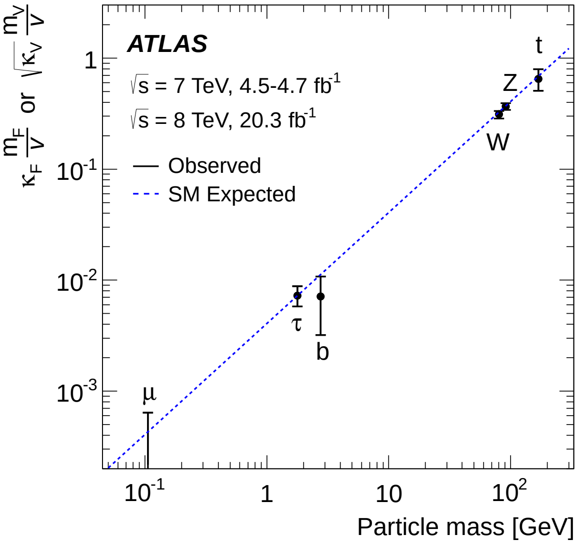

Figure 12.2: Measurements of the reduced coupling-strength scale factors $y_V = \sqrt{\kappa_V}\frac{m_V}{v}$ for the vector bosons and $y_f = \kappa_f \frac{m_f}{v}$ as a function of the particle mass (black dots) assuming an SM Higgs boson with a mass of 125.36 GeV. Here v is the Higgs vacuum expectation value, and $\kappa_{V/f}$ the measured coupling strength divided by SM predicted coupling strength. The square root for the vector boson coupling reflects the relationship between vector boson masses and coupling strength in the Higgs Lagrangian. Comparison to SM prediction as blue dashed line [78].

Appendix A

Fits of the Background Model to Data

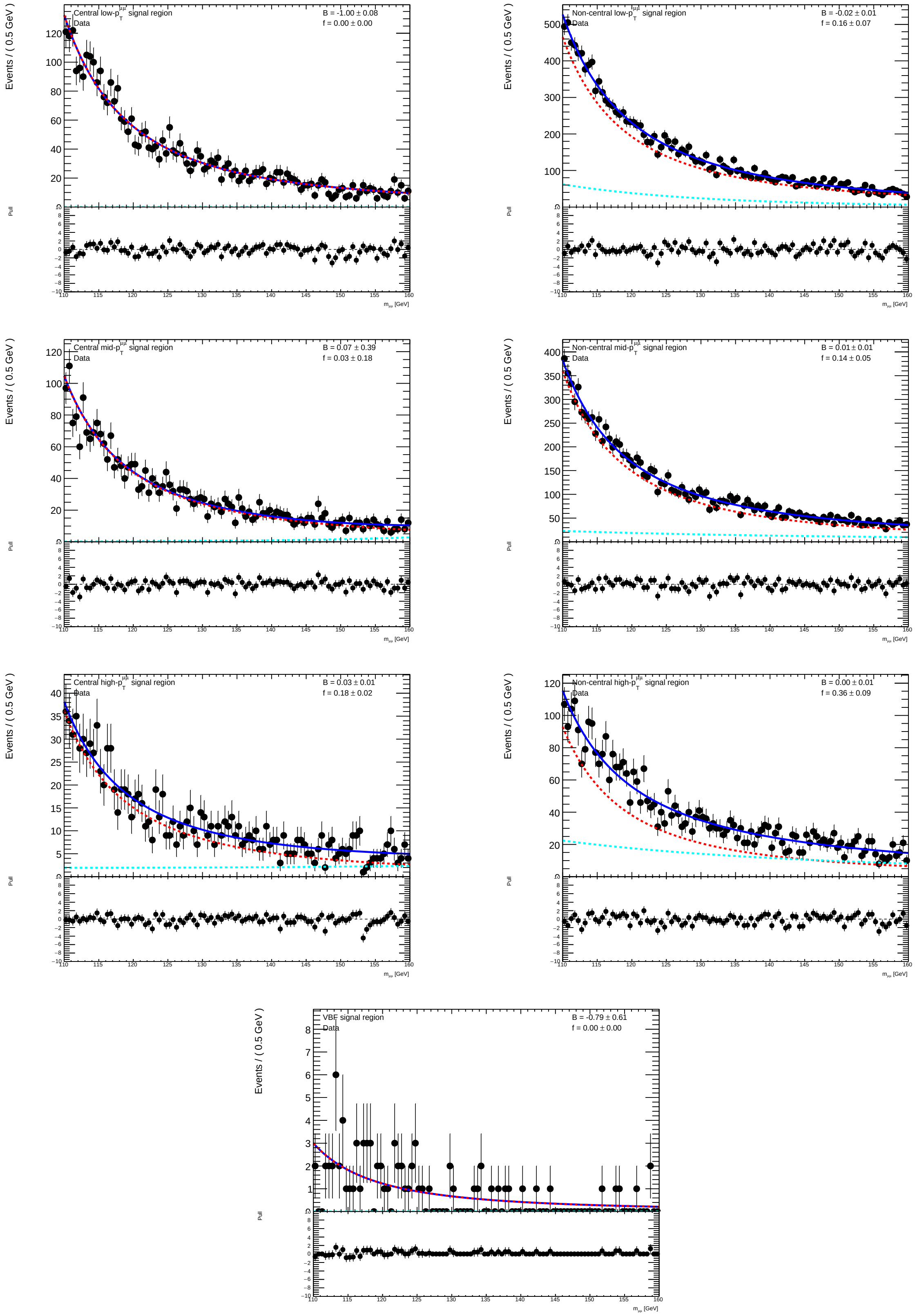

Figure A.1: Fit of the background model (solid blue line) to data (black dots) in the upper part of each plot, pull between model and data in the lower part of each plot, shown for all seven signal regions. Shown separately are the Breit-Wigner term (dashed red line) and the exponential term (dashed turquoise line).

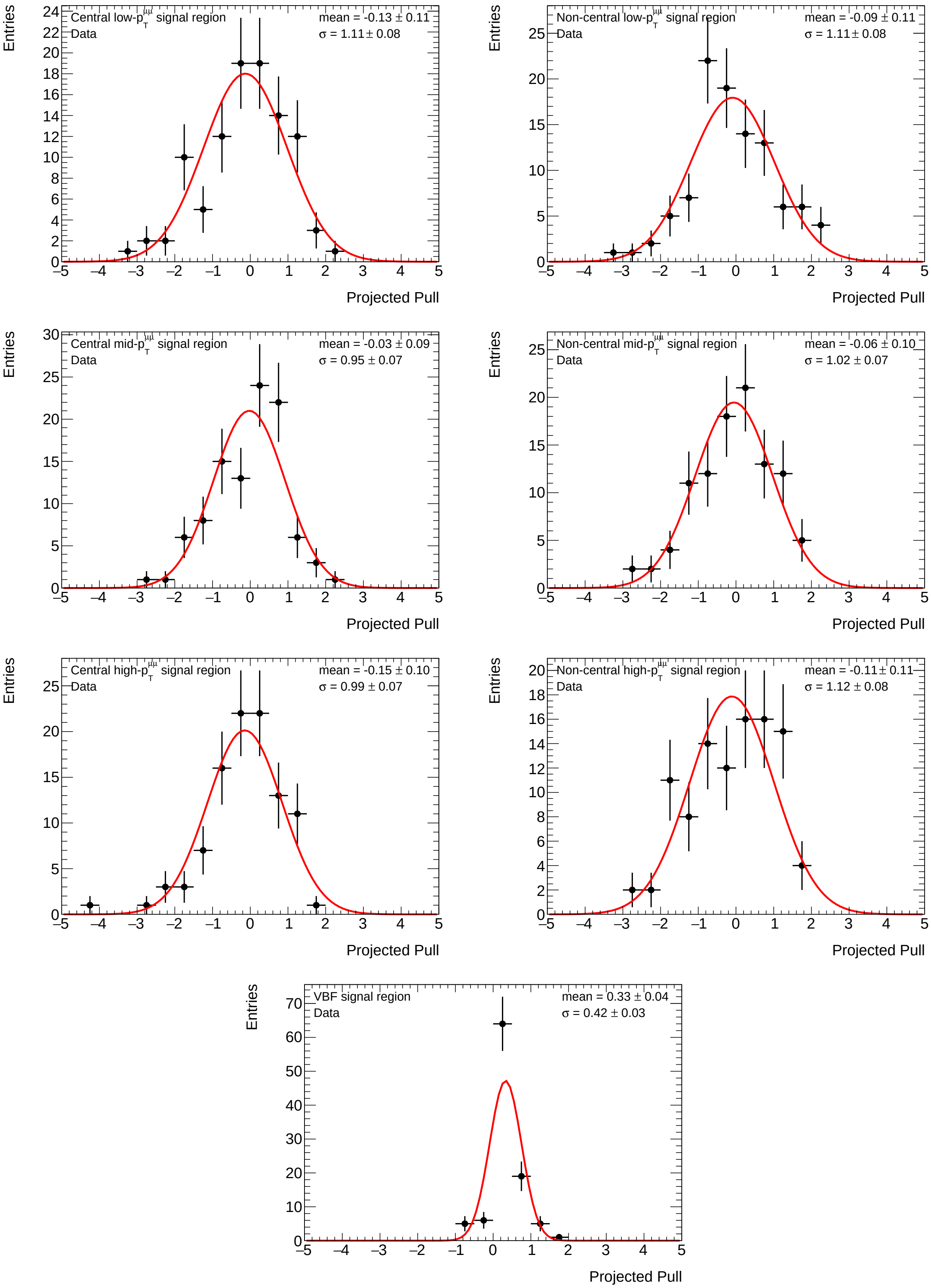

Figure A.2: Distribution of the pulls between background fit and data (black) and fit of normal distribution to pull distribution (red line)

Appendix B

Exclusion Limits

$m_{\rm H}$ [GeV]	obs. limit.	exp. media	exp. $+2\sigma$	exp. $+1\sigma$	exp. -1σ	exp. -2σ
115	27.4	43.4	81.5	60.5	31.2	23.3
116	12.9	19.6	36.7	27.2	14.1	10.5
117	9.4	13.7	25.7	19.0	9.8	7.3
118	8.0	11.1	20.9	15.5	8.0	6.0
119	7.3	9.8	18.4	13.6	7.1	5.3
120	7.1	9.1	17.1	12.6	6.5	4.9
121	7.1	8.7	16.4	12.1	6.3	4.7
122	7.3	8.6	16.1	11.9	6.2	4.6
123	7.6	8.6	16.2	11.9	6.2	4.6
124	8.1	8.8	16.5	12.2	6.3	4.7
125	8.7	9.1	17.1	12.6	6.5	4.9
126	9.4	9.5	17.9	13.2	6.8	5.1
127	10.2	10.0	18.8	13.9	7.2	5.3
128	11.1	10.6	20.0	14.7	7.6	5.6
129	12.1	11.2	21.2	15.6	8.1	6.0
130	13.1	11.9	22.6	16.6	8.6	6.4
131	14.2	12.7	24.0	17.7	9.1	6.8
132	15.3	13.4	25.4	18.7	9.7	7.2
133	16.3	14.2	26.8	19.7	10.2	7.6
134	17.2	14.8	28.1	20.7	10.7	7.9
135	18.0	15.4	29.1	21.4	11.1	8.2
136	18.6	15.8	30.0	22.0	11.4	8.4
137	19.1	16.1	30.6	22.5	11.6	8.6
138	19.5	16.4	31.0	22.9	11.8	8.7
139	19.8	16.6	31.4	23.1	12.0	8.9
140	20.1	16.9	31.9	23.5	12.1	9.0
141	20.5	17.2	32.7	24.1	12.4	9.2
142	21.2	18.0	34.1	25.1	13.	9.6
143	22.5	19.2	36.4	26.8	13.9	10.0
144	25.0	21.5	40.8	30.0	15.5	11.2
145	29.6	26.0	49.3	36.3	18.8	13.9

Table B.1: Observed and expected 95% CL upper limits on H $\rightarrow$ $\mu\mu$ signal strength, including expected limit $\pm1\sigma$ and $\pm2\sigma$ uncertainties.

Bibliography

[1] **OPAL, DELPHI, LEP Working Group for Higgs boson searches, ALEPH, L3** Collaboration, R. Barate *et al.*, "Search for the standard model Higgs boson at LEP," *Phys. Lett.* **B565** (2003) 61–75, `arXiv:hep-ex/0306033 [hep-ex]`.

[2] **ATLAS** Collaboration, G. Aad *et al.*, "Observation of a new particle in the search for the Standard Model Higgs boson with the ATLAS detector at the LHC," *Phys. Lett.* **B716** (2012) 1–29, `arXiv:1207.7214 [hep-ex]`.

[3] **CMS** Collaboration, S. Chatrchyan *et al.*, "Observation of a new boson at a mass of 125 GeV with the CMS experiment at the LHC," *Phys. Lett.* **B716** (2012) 30–61, `arXiv:1207.7235 [hep-ex]`.

[4] **ATLAS, CMS** Collaboration, G. Aad *et al.*, "Combined Measurement of the Higgs Boson Mass in pp Collisions at $\sqrt{s} = 7$ and 8 TeV with the ATLAS and CMS Experiments," *Phys. Rev. Lett.* **114** (2015) 191803, `arXiv:1503.07589 [hep-ex]`.

[5] **ATLAS, CMS** Collaboration, G. Aad *et al.*, "Measurements of the Higgs boson production and decay rates and constraints on its couplings from a combined ATLAS and CMS analysis of the LHC pp collision data at $\sqrt{s} = 7$ and 8 TeV," *JHEP* **08** (2016) 045, `arXiv:1606.02266 [hep-ex]`.

[6] **ATLAS** Collaboration, G. Aad *et al.*, "Search for the Standard Model Higgs boson decay to $\mu^+\mu^-$ with the ATLAS detector," *Phys. Lett.* **B738** (2014) 68–86, `arXiv:1406.7663 [hep-ex]`.

[7] **CMS** Collaboration, V. Khachatryan *et al.*, "Search for a standard model-like Higgs boson in the $\mu^+\mu^-$ and e^+e^- decay channels at the LHC," *Phys. Lett.* **B744** (2015) 184–207, `arXiv:1410.6679 [hep-ex]`.

[8] C. P. Burgess and G. D. Moore, *The standard model: A primer*. Cambridge University Press, 2006.

[9] S. L. Glashow, "Partial Symmetries of Weak Interactions," *Nucl. Phys.* **22** (1961) 579–588.

[10] J. R. Oppenheimer *et al.*, “Strange particles and weak interactions,” in *Proceedings, 7th Annual Conference on High Energy Nuclear Physics: Rochester, New York, USA, April 15-19, 1957*, pp. IX.1–52. 1957. `https://inspirehep.net/record/1280823/files/c57-04-15-pIX.pdf`.

[11] S. Weinberg, “A Model of Leptons,” *Phys. Rev. Lett.* **19** (1967) 1264–1266.

[12] D. J. Gross and F. Wilczek, “Ultraviolet Behavior of Nonabelian Gauge Theories,” *Phys. Rev. Lett.* **30** (1973) 1343–1346.

[13] H. D. Politzer, “Reliable Perturbative Results for Strong Interactions?,” *Phys. Rev. Lett.* **30** (1973) 1346–1349.

[14] F. Englert and R. Brout, “Broken Symmetry and the Mass of Gauge Vector Mesons,” *Phys. Rev. Lett.* **13** (1964) 321–323.

[15] P. W. Higgs, “Broken Symmetries and the Masses of Gauge Bosons,” *Phys. Rev. Lett.* **13** (1964) 508–509.

[16] G. S. Guralnik, C. R. Hagen, and T. W. B. Kibble, “Global Conservation Laws and Massless Particles,” *Phys. Rev. Lett.* **13** (1964) 585–587.

[17] **Particle Data Group** Collaboration, C. Patrignani *et al.*, “Review of Particle Physics,” *Chin. Phys.* **C40** no. 10, (2016) 100001.

[18] D. Griffiths, *Introduction to elementary particles.* 2008.

[19] A. Djouadi, “The Anatomy of electro-weak symmetry breaking. I: The Higgs boson in the standard model,” *Phys. Rept.* **457** (2008) 1–216, `arXiv:hep-ph/0503172 [hep-ph]`.

[20] J. D. Lykken, “Beyond the Standard Model,” in *CERN Yellow Report CERN-2010-002, 101-109.* 2010. `arXiv:1005.1676 [hep-ph]`. `http://lss.fnal.gov/cgi-bin/find_paper.pl?conf-10-103`.

[21] A. Dery, A. Efrati, Y. Hochberg, and Y. Nir, “What if $BR(h \to \mu\mu)/BR(h \to \tau\tau)$ does not equal m_μ^2/m_τ^2?,” *JHEP* **05** (2013) 039, `arXiv:1302.3229 [hep-ph]`.

[22] L. Evans and P. Bryant, “LHC Machine,” *JINST* **3** (2008) S08001.

[23] C. Lefèvre, “The CERN accelerator complex. Complexe des accélérateurs du CERN.” Dec, 2008.

[24] **ATLAS** Collaboration, G. Aad *et al.*, “Improved luminosity determination in pp collisions at sqrt(s) = 7 TeV using the ATLAS detector at the LHC,” *Eur. Phys. J.* **C73** no. 8, (2013) 2518, `arXiv:1302.4393 [hep-ex]`.

[25] S. White, “Luminosity Scans at the LHC. Luminosity Scans at LHC,”. `https://cds.cern.ch/record/1357865`.

[26] W. Stirling, “Private communication,”.

[27] **ATLAS** Collaboration, G. Aad *et al.*, “The ATLAS Experiment at the CERN Large Hadron Collider,” *JINST* **3** (2008) S08003.

[28] J. Pequenao, “Computer generated image of the whole ATLAS detector.” Mar, 2008.

[29] **ATLAS** Collaboration, “ATLAS magnet system: Technical design report,”.

[30] R. L. Gluckstern, “Uncertainties in track momentum and direction, due to multiple scattering and measurement errors,” *Nuclear Instruments and Methods* **24** (July, 1963) 381–389.

[31] **ATLAS TRT** Collaboration, E. Abat *et al.*, “The ATLAS Transition Radiation Tracker (TRT) proportional drift tube: Design and performance,” *JINST* **3** (2008) P02013.

[32] K. Potamianos, “The upgraded Pixel detector and the commissioning of the Inner Detector tracking of the ATLAS experiment for Run-2 at the Large Hadron Collider,” *PoS* **EPS-HEP2015** (2015) 261, `arXiv:1608.07850 [physics.ins-det]`.

[33] **ATLAS** Collaboration, “ATLAS liquid argon calorimeter: Technical design report,”.

[34] J. Pequenao, “Computer Generated image of the ATLAS calorimeter.” Mar, 2008.

[35] **ATLAS** Collaboration, “ATLAS muon spectrometer: Technical design report,”.

[36] A. Ruiz-Martinez and A. Collaboration, “The Run-2 ATLAS Trigger System,” Tech. Rep. ATL-DAQ-PROC-2016-003, CERN, Geneva, Feb, 2016. `https://cds.cern.ch/record/2133909`.

[37] J. Glatzer, “Operation of the Upgraded ATLAS Level-1 Central Trigger System,” *J. Phys. Conf. Ser.* **664** no. 8, (2015) 082013.

[38] “Wlcg website: Tier centres.” `http://wlcg-public.web.cern.ch/tier-centres`.

[39] C. Serfon, M. Barisits, T. Beermann, V. Garonne, L. Goossens, M. Lassnig, A. Nairz, and R. Vigne, “Rucio, the next-generation Data Management system in ATLAS,” Tech. Rep. ATL-SOFT-PROC-2014-009, CERN, Geneva, Oct, 2014. `https://cds.cern.ch/record/1955476`.

[40] **LHC Higgs Cross Section Working Group** Collaboration, J. R. Andersen *et al.*, “Handbook of LHC Higgs Cross Sections: 3. Higgs Properties,” `arXiv:1307.1347 [hep-ph]`.

[41] S. Dittmaier *et al.*, “Handbook of LHC Higgs Cross Sections: 2. Differential Distributions,” `arXiv:1201.3084 [hep-ph]`.

[42] S. Frixione, P. Nason, and C. Oleari, “Matching NLO QCD computations with Parton Shower simulations: the POWHEG method,” *JHEP* **11** (2007) 070, `arXiv:0709.2092 [hep-ph]`.

[43] H.-L. Lai, M. Guzzi, J. Huston, Z. Li, P. M. Nadolsky, J. Pumplin, and C. P. Yuan, “New parton distributions for collider physics,” *Phys. Rev.* **D82** (2010) 074024, `arXiv:1007.2241 [hep-ph]`.

[44] T. Sjostrand, S. Mrenna, and P. Z. Skands, “A Brief Introduction to PYTHIA 8.1,” *Comput. Phys. Commun.* **178** (2008) 852–867, `arXiv:0710.3820 [hep-ph]`.

[45] D. de Florian, G. Ferrera, M. Grazzini, and D. Tommasini, “Higgs boson production at the LHC: transverse momentum resummation effects in the H-¿2gamma, H-¿WW-¿lnu lnu and H-¿ZZ-¿4l decay modes,” *JHEP* **06** (2012) 132, `arXiv:1203.6321 [hep-ph]`.

[46] M. Grazzini and H. Sargsyan, “Heavy-quark mass effects in Higgs boson production at the LHC,” *JHEP* **09** (2013) 129, `arXiv:1306.4581 [hep-ph]`.

[47] B. Mellado Garcia, P. Musella, M. Grazzini, and R. Harlander, “CERN Report 4: Part I Standard Model Predictions,”. `https://cds.cern.ch/record/2150771`.

[48] U. Aglietti, R. Bonciani, G. Degrassi, and A. Vicini, “Two loop light fermion contribution to Higgs production and decays,” *Phys. Lett.* **B595** (2004) 432–441, `arXiv:hep-ph/0404071 [hep-ph]`.

[49] S. Actis, G. Passarino, C. Sturm, and S. Uccirati, “NLO Electroweak Corrections to Higgs Boson Production at Hadron Colliders,” *Phys. Lett.* **B670** (2008) 12–17, `arXiv:0809.1301 [hep-ph]`.

[50] M. Ciccolini, A. Denner, and S. Dittmaier, “Strong and electroweak corrections to the production of Higgs + 2jets via weak interactions at the LHC,” *Phys. Rev. Lett.* **99** (2007) 161803, `arXiv:0707.0381 [hep-ph]`.

[51] M. Ciccolini, A. Denner, and S. Dittmaier, “Electroweak and QCD corrections to Higgs production via vector-boson fusion at the LHC,” *Phys. Rev.* **D77** (2008) 013002, `arXiv:0710.4749 [hep-ph]`.

[52] K. Arnold *et al.*, “VBFNLO: A Parton level Monte Carlo for processes with electroweak bosons,” *Comput. Phys. Commun.* **180** (2009) 1661–1670, `arXiv:0811.4559 [hep-ph]`.

[53] P. Bolzoni, F. Maltoni, S.-O. Moch, and M. Zaro, "Higgs production via vector-boson fusion at NNLO in QCD," *Phys. Rev. Lett.* **105** (2010) 011801, `arXiv:1003.4451 [hep-ph]`.

[54] A. Djouadi, J. Kalinowski, and M. Spira, "HDECAY: A Program for Higgs boson decays in the standard model and its supersymmetric extension," *Comput. Phys. Commun.* **108** (1998) 56–74, `arXiv:hep-ph/9704448 [hep-ph]`.

[55] J. Alwall, M. Herquet, F. Maltoni, O. Mattelaer, and T. Stelzer, "MadGraph 5 : Going Beyond," *JHEP* **06** (2011) 128, `arXiv:1106.0522 [hep-ph]`.

[56] R. D. Ball *et al.*, "Parton distributions with LHC data," *Nucl. Phys.* **B867** (2013) 244–289, `arXiv:1207.1303 [hep-ph]`.

[57] T. Sjostrand, S. Mrenna, and P. Z. Skands, "PYTHIA 6.4 Physics and Manual," *JHEP* **05** (2006) 026, `arXiv:hep-ph/0603175 [hep-ph]`.

[58] T. Gleisberg, S. Hoeche, F. Krauss, M. Schonherr, S. Schumann, F. Siegert, and J. Winter, "Event generation with SHERPA 1.1," *JHEP* **02** (2009) 007, `arXiv:0811.4622 [hep-ph]`.

[59] **ATLAS** Collaboration, G. Aad *et al.*, "The ATLAS Simulation Infrastructure," *Eur. Phys. J.* **C70** (2010) 823–874, `arXiv:1005.4568 [physics.ins-det]`.

[60] **GEANT4** Collaboration, S. Agostinelli *et al.*, "GEANT4: A Simulation toolkit," *Nucl. Instrum. Meth.* **A506** (2003) 250–303.

[61] **ATLAS** Collaboration, I. Chalupkova, "Inner tracking performance in ATLAS: vertex and mass resolution," *PoS* **Beauty2013** (2013) 069.

[62] **ATLAS** Collaboration, G. Aad *et al.*, "Muon reconstruction performance of the ATLAS detector in proton–proton collision data at $\sqrt{s}$=13 TeV," `arXiv:1603.05598 [hep-ex]`.

[63] **ATLAS** Collaboration, G. Aad *et al.*, "Measurement of the muon reconstruction performance of the ATLAS detector using 2011 and 2012 LHC proton–proton collision data," *Eur. Phys. J.* **C74** no. 11, (2014) 3130, `arXiv:1407.3935 [hep-ex]`.

[64] "Muon reconstruction performance in early $\sqrt{}$ s=13 TeV data," Tech. Rep. ATL-PHYS-PUB-2015-037, CERN, Geneva, Aug, 2015. `https://cds.cern.ch/record/2047831`.

[65] M. Cacciari, G. P. Salam, and G. Soyez, "The Anti-k(t) jet clustering algorithm," *JHEP* **04** (2008) 063, `arXiv:0802.1189 [hep-ph]`.

[66] A. Collaboration, "Selection of jets produced in 13TeV proton-proton collisions with the ATLAS detector," Tech. Rep. ATLAS-COM-CONF-2015-024, CERN, Geneva, May, 2015. `https://cds.cern.ch/record/2016323`.

[67] "Tagging and suppression of pileup jets with the ATLAS detector," Tech. Rep. ATLAS-CONF-2014-018, CERN, Geneva, May, 2014. `https://cds.cern.ch/record/1700870`.

[68] "Expected performance of the ATLAS b-tagging algorithms in Run-2," Tech. Rep. ATL-PHYS-PUB-2015-022, CERN, Geneva, Jul, 2015. `http://cds.cern.ch/record/2037697`.

[69] **ATLAS** Collaboration, G. Aad *et al.*, "Performance of b-Jet Identification in the ATLAS Experiment," `arXiv:1512.01094 [hep-ex]`.

[70] L. Demortier and L. Lyons, "Everything you always wanted to know about pulls," Tech. Rep. CDF/ANAL/PUBLIC/5776, CDF, February, 2002.

[71] **LHC Higgs Cross Section Working Group** Collaboration, S. Dittmaier *et al.*, "Handbook of LHC Higgs Cross Sections: 1. Inclusive Observables," `arXiv:1101.0593 [hep-ph]`.

[72] "Jet Calibration and Systematic Uncertainties for Jets Reconstructed in the ATLAS Detector at $\sqrt{s} = 13$ TeV," Tech. Rep. ATL-PHYS-PUB-2015-015, CERN, Geneva, Jul, 2015. `https://cds.cern.ch/record/2037613`.

[73] "Expected performance of missing transverse momentum reconstruction for the ATLAS detector at $\sqrt{s} = 13$ TeV," Tech. Rep. ATL-PHYS-PUB-2015-023, CERN, Geneva, Jul, 2015. `https://cds.cern.ch/record/2037700`.

[74] G. Cowan, K. Cranmer, E. Gross, and O. Vitells, "Asymptotic formulae for likelihood-based tests of new physics," *Eur. Phys. J.* **C71** (2011) 1554, `arXiv:1007.1727 [physics.data-an]`. [Erratum: Eur. Phys. J.C73,2501(2013)].

[75] A. L. Read, "Presentation of search results: The CL(s) technique," *J. Phys.* **G28** (2002) 2693–2704. [,11(2002)].

[76] C. Campagnari and M. Franklin, "The Discovery of the top quark," *Rev. Mod. Phys.* **69** (1997) 137–212, `arXiv:hep-ex/9608003 [hep-ex]`.

[77] **DONUT** Collaboration, K. Kodama *et al.*, "Observation of tau neutrino interactions," *Phys. Lett.* **B504** (2001) 218–224, `arXiv:hep-ex/0012035 [hep-ex]`.

[78] **ATLAS** Collaboration, G. Aad *et al.*, "Measurements of the Higgs boson production and decay rates and coupling strengths using pp collision data at $\sqrt{s} = 7$ and 8 TeV in the ATLAS experiment," *Eur. Phys. J.* **C76** no. 1, (2016) 6, `arXiv:1507.04548 [hep-ex]`.

[79] **ATLAS** Collaboration, T. A. collaboration, "Search for Higgs bosons decaying into di-muon in pp collisions at $\sqrt{s} = 13$ TeV with the ATLAS detector,".

Danksagung

Besonders bedanken möchte ich mich bei

- Prof. Dr. Dorothee Schaile für die Möglichkeit dieses Promotionsstudiums und die vorlaufende Unterstützung
- Prof. Dr. Thomas Kuhr für das Erstellen des Zweitgutachtens
- Dr. Elmsheuser und Dr. Duckeck für ihre Hilfe und Betreuung über die Jahre
- Allen jetzigen und ehemaligen Mitgliedern des Lehrstuhl Schaile, allesamt verantwortlich für ein immer gutes Lehrstuhlklima.